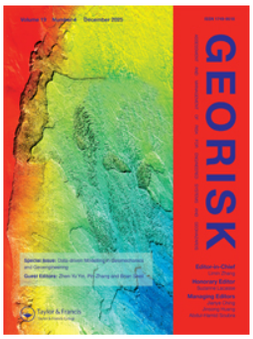

Taylor & Francis
Taylor & Francis Group

Georisk: Assessment and Management of Risk for Engineered Systems and Geohazards

ISSN: 1749-9518 (Print) 1749-9526 (Online) Journal homepage: www.tandfonline.com/journals/ngrk20

Site-specific projection of rainfall patterns under climate change by joint sparse representation

Tianyang Lu, Yu Wang, Zheng Guan & Kostas Senetakis

To cite this article: Tianyang Lu, Yu Wang, Zheng Guan & Kostas Senetakis (20 Jan 2026): Site-specific projection of rainfall patterns under climate change by joint sparse representation, Georisk: Assessment and Management of Risk for Engineered Systems and Geohazards, DOI: 10.1080/17499518.2026.2616772

To link to this article: https://doi.org/10.1080/17499518.2026.2616772

Published online: 20 Jan 2026.

GEORISK
https://doi.org/10.1080/17499518.2026.2616772

Taylor & Francis
Taylor & Francis Group

Site-specific projection of rainfall patterns under climate change by joint sparse representation

Tianyang Lu[a], Yu Wang [b], Zheng Guan[c] and Kostas Senetakis[d]

[a]Department of Architecture and Civil Engineering, City University of Hong Kong, Kowloon, Hong Kong, People's Republic of China; [b]State Key Laboratory of Climate Resilience for Coastal Cities, Department of Civil and Environmental Engineering, The Hong Kong University of Science and Technology, Kowloon, Hong Kong, People's Republic of China; [c]Faculty of Civil Engineering and Geoscience, Delft University of Technology, Delft, the Netherlands; [d]Department of Architecture and Civil Engineering, City University of Hong Kong, Kowloon, Hong Kong, People's Republic of China

ABSTRACT

As climate change alters global rainfall patterns, many regions are facing increased intensity and frequency of rainfall events. These changes pose significant risks to civil infrastructure, which was often designed based on historical data and may no longer be resilient. Rainfall-induced failures can lead to severe, life-threatening consequences. Local factors, such as topography and elevation, greatly influence rainfall variability, making site-specific projections essential for effective risk assessment of infrastructure. However, current rainfall projections from General Circulation Models (GCMs) have coarse spatial resolutions (e.g. 100 km), which are inadequate for assessing risks at specific sites, such as slopes near railways, where the relevant scale is often tens to hundreds of metres. This study proposes an innovative method that integrates historical rainfall records with GCM projections using a joint sparse representation (JSR) framework to project future rainfall patterns at specific sites. This approach combines regional trends from GCMs with local data to maintain regional consistency while accurately reflecting local characteristics. A temporal downscaling step further enhances the resolution for engineering applications. The method is demonstrated using real rain gauge data from Hong Kong.

ARTICLE HISTORY
Received 21 September 2025
Accepted 8 January 2026

KEYWORDS
Climate change; future rainfall pattern; joint sparse representation; site-specific projection; Bayesian inference

1. Introduction

The Intergovernmental Panel on Climate Change (IPCC) has repeatedly highlighted alarming trends of global warming, projecting a significant rise in average global temperatures by the end of this century (IPCC 2023). Rising temperatures intensify evaporation, which subsequently alters atmospheric moisture content and influences global rainfall patterns (Masson-Delmotte et al. 2021). These shifts in the hydrological cycle contribute to significant changes in precipitation intensity and distribution, attracting increasing attention globally. To predict these climate change-induced alterations in meteorological phenomena, the Coupled Model Intercomparison Project (CMIP) developed General Circulation Models (GCMs) and simulated atmospheric and oceanic processes under different climate scenarios (Durack et al. 2025). These models incorporate both natural and human influences on climate systems, providing projections of temperature, precipitation and other climate variables with a spatial resolution of tens or hundreds of km (Bader et al. 2008). The predicted rainfall patterns indicate that extreme rainfall events have already intensified in many regions and are projected to increase further, posing significant risks to human settlements and infrastructure (IPCC 2023). For example, prolonged and intense rainfall may overwhelm existing drainage systems, increase flooding risks and trigger landslides, due to soil saturation and reduced shear strength of soil, especially in hilly areas (Gao et al. 2023; Oguz et al. 2024). These hazards might further damage buildings, roads, bridges and disrupt transportation, leading to economic losses and threats to human safety (Gofar and Lee 2008). Past events have highlighted the severe consequences of such rainfall-induced disasters. For example, the 2008 floods and landslides in Santa Catarina, Brazil, triggered by extreme rainfall, resulted in over 135 fatalities and caused an economic loss exceeding US$1.4 billion (Xavier, Barcellos, and de Freitas 2014). Similarly, in September 2023, Hong Kong experienced

CONTACT Yu Wang wang.yu@ust.hk State Key Laboratory of Climate Resilience for Coastal Cities, Department of Civil and Environmental Engineering, The Hong Kong University of Science and Technology, Clear Water Bay, Kowloon, Hong Kong, People's Republic of China

its most intense rainfall in nearly 140 years, leading to widespread flooding, landslides and severe disruptions to transportation and infrastructure. The event resulted in at least two fatalities, over 140 injuries and significant economic losses due to infrastructure destruction, public transportation shutdowns and widespread business closures (Wong, Fan, and Yeung 2024). In addition, the impacts of climate change exhibit spatial heterogeneity and the variance of rainfall has increased under changing climate conditions (Braga and Laurini 2024; Dore 2005; Ohba and Sugimoto 2019). In May 2024, Hong Kong experienced an intense rainfall event that was concentrated in the Sai Kung area, causing severe landslides and road closures (Leung 2024). Given the severe consequences and increasing possibility of such events, it is crucial to reassess and adapt existing infrastructures, based on projections of future rainfall patterns, to enhance urban resilience and safety (Nissen and Ulbrich 2017).

As rainfall patterns may vary significantly even at sub-kilometre scales due to local factors like topography, land use and atmospheric processes (Fiener and Auerswald 2009), localised rainfall variations have a direct impact on the assessment of rainfall-induced risk. Infrastructure systems, particularly slopes, drainage and transportation networks, are highly sensitive to rainfall intensity, therefore demanding an accurate estimate of rainfall patterns at specific sites. For example, Hong Kong maintains a dense rain gauge network with an average station density of one station per approximately 5.7 km^2, enabling detailed local-scale monitoring (Drainage Services Department 2018). In some areas, particularly those prone to landslides, the gauge density is even higher to ensure close monitoring of extreme precipitation. Records of rain gauges that are located within a few hundred metres to a few kilometres are often used for risk assessment of rainfall-induced landslides at a specific slope. For example, Figure 1(a) presents the location of rain gauge N05, which is situated approximately 1.3 km from an illustrative slope that will be discussed later in this study. Due to its close proximity, the data collected from this rain gauge is considered representative of the rainfall conditions at the slope. This gauge has hourly rainfall data monitored for the past decades, but the future rainfall pattern at N05 is expected to vary due to climate change. For example, Figure 1(b) shows the projection from a GCM called ACCESS-CM2 model, indicating that rainfall pattern changes in the area encompassing rain gauge N05. Note that the spatial resolution of rainfall data from GCMs, such as the ACCESS-CM2 model, is as large as a longitude of 1.875° by a latitude of 1.25°. Such a spatial resolution is even larger than the entire area of Hong Kong. In addition, the temporal resolution (e.g. monthly) of rainfall data from GCMs is too low and not suitable for drainage design or slope stability assessment. In other words, GCM projection results are of low spatial and temporal resolutions and they cannot be directly used to represent the site-specific rainfall patterns required for engineering applications. This underscores an important research gap and question: how to project future rainfall patterns at a specific site under climate change and ensure that the projected rainfall patterns are consistent with both regional projections (e.g. GCMs) and historical rainfall data observed at the specific site?

Various methods have been proposed in the literature to improve the spatial or temporal resolution of rainfall pattern projections. In general, existing spatial downscaling approaches fall into two main categories: dynamical and statistical downscaling (Maraun et al. 2010). Although dynamical downscaling incorporates boundary conditions from GCMs and ensures physical consistency (Mayer et al. 2022), it is computationally intensive and its spatial resolution (e.g. 50 km for Euro-CORDEX) remains insufficient for site-specific applications such as slope stability analysis. Statistical downscaling is based on the assumption that large-scale climate variables simulated by global or regional climate models (GCMs/RCMs) contain useful information about local-scale processes. Therefore, a statistical or empirical relationship can be established between large-scale atmospheric predictors and local-scale rainfall. These relationships are learned from historical data and applied to model output to obtain downscaled projections (Bürger et al. 2012; Dhanapala Arachchige et al. 2014; Jeong et al. 2012; Wilby et al. 2004; Wong et al. 2014). Although statistical downscaling is theoretically useful to site-specific applications, its effectiveness and robustness depend critically on the availability of reliable and spatially dense observational data for model calibration and validation (Maraun et al. 2010; Wilby and Wigley 1997).

Limited previous studies have applied statistical spatial downscaling of rainfall at a specific site to assess its impact on slope stability. For example, Dehn et al. (2000) employed a transfer function with bounded error, while Collison et al. (2000) used a simple correction factor to adjust rainfall. Martel et al. (2021) and Liu and Wang (2024) altered future rainfall Intensity – Duration – Frequency (IDF) curves by applying scaling factors to adjust projected rainfall intensities under future climate scenarios. Oguz et al. (2024) derived key statistical parameters of rainfall, such as wet-day mean from

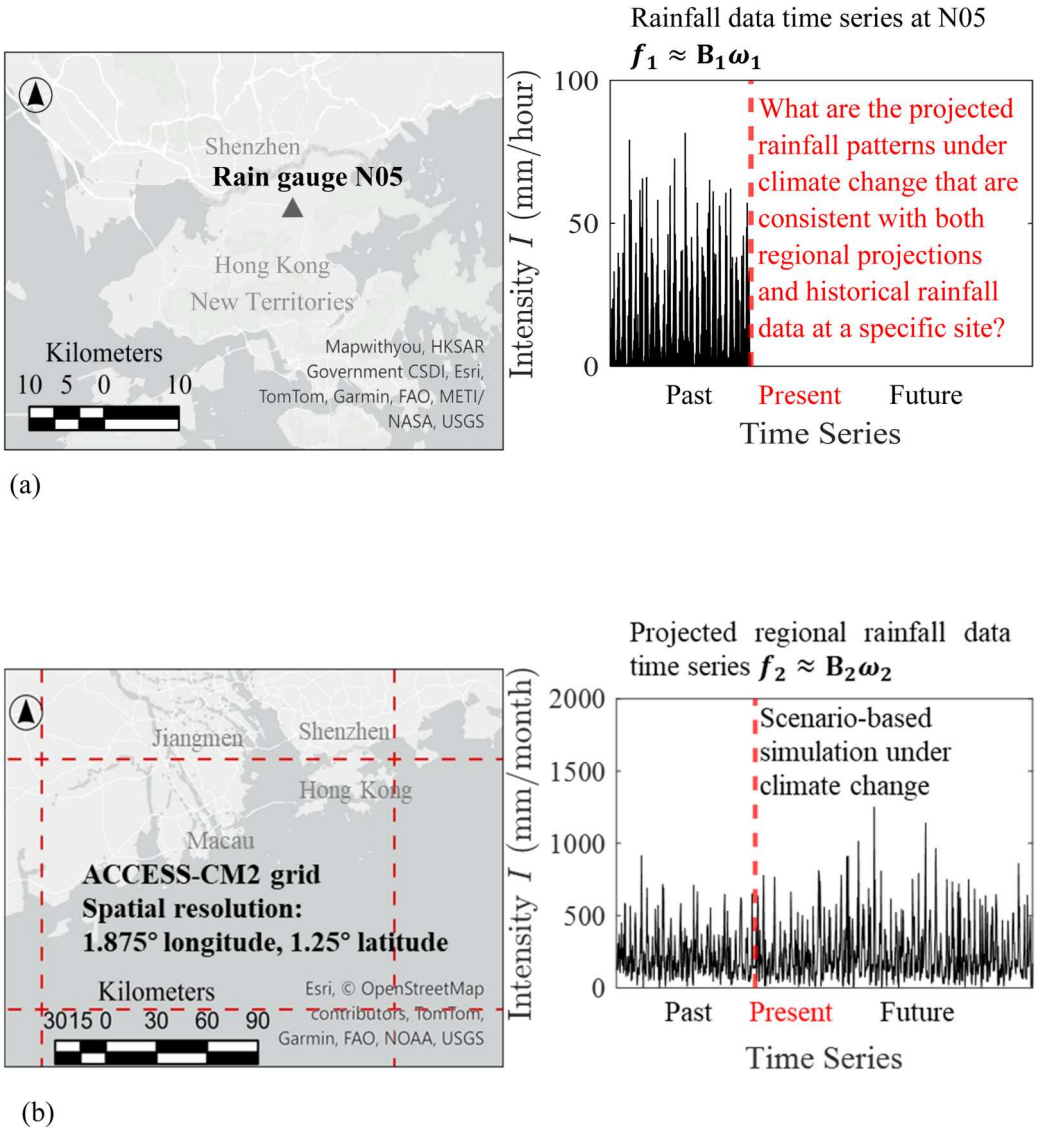

Figure 1. An illustration of rainfall patterns from observations and GCMs in Hong Kong (a) An illustration of high-temporal-resolution (mm/hour) rainfall records measured by a rain gauge (N05) at a specific site (b) An illustration of regional GCM rainfall projection with low temporal (mm/month) and spatial resolutions.

RCM outputs under future climate scenarios and updated the IDF curves accordingly. These methods typically rely on empirical relationships between large-scale climate predictors and local-scale rainfall patterns developed from past observations, which may not be valid under non-stationary changes of climate conditions. In addition, some of these methods cannot generate localised hourly rainfall time series. Therefore, they might underestimate the complex spatial and temporal variability of rainfall. Their flexibility might also be limited, as they often prioritised replicating and adjusting historical records, rather than capturing the trend under climate change and temporal variability of future site-specific rainfall patterns. In short, they are not explicitly designed to simultaneously preserve the local characteristics of rainfall patterns while ensuring consistency with the projected regional changes.

Moreover, spatial downscaling results are often available only at low temporal resolutions (e.g. monthly), whereas engineering applications typically require rainfall events at an hourly time scale, making temporal downscaling necessary (Segond et al. 2007; Drainage Services Department 2018; Gariano et al. 2020; Acharya et al. 2022). Various approaches, such as multiplicative cascade models (Förster et al. 2016; Müller and Haberlandt 2018), the method of fragments (Westra et al. 2012) and stochastic storm selection (Socolofsky et al. 2001; Koutsoyiannis and Onof 2003; Takhellambam et al. 2022),

have been developed to generate hourly rainfall for engineering applications.

To project future rainfall patterns with an hourly temporal resolution at a specific site under climate change, this study proposes a joint sparse representation (JSR) formulation, which fuses regional GCM projections with historical rainfall observations at a specific site for spatial downscaling and employs a stochastic storm selection method for temporal downscaling. The proposed framework generates hourly, site-specific rainfall projections that are consistent with regional climate trends while capturing local spatial variability and realistic temporal event structures. Such detailed and site-tailored rainfall projections are essential for infrastructure adaptation and risk assessment under changing climate conditions. After the introduction, Section 2 outlines the overall framework of the proposed approach, including both spatial and temporal downscaling. Section 3 presents the concept of the JSR framework for spatial downscaling and details of the proposed methodology. Section 4 introduces the stochastic storm selection method for temporal downscaling. Section 5 details the implementation procedure. Section 6 demonstrates the effectiveness of the proposed method through a real case study and presents the projected future rainfall patterns at the specific site. Section 7 illustrates an application of downscaled future rainfall projections to an example of landslide hazard assessment, showing how rainfall patterns with high spatial and temporal resolutions influence slope stability. Finally, Section 8 summarises the key findings of the study.

2. Framework for projecting site-specific rainfall patterns under climate change

As shown in Figure 2, the proposed framework consists of two sequential components. First, a JSR-based method is proposed for spatial downscaling, which takes site-specific rainfall observations and GCM rainfall projections with low spatial and temporal resolutions as inputs and projects site-specific rainfall data time series at a low temporal resolution (e.g. monthly). This output then provides the basis for the second component, temporal downscaling, which combines the site-specific low-resolution projections with site-specific historical rainfall data with a high temporal resolution to generate the final site-specific projected rainfall events with a high temporal resolution (e.g. hourly) required for engineering applications.

To further illustrate the characteristics of the data involved in the framework, Figure 1 shows that the rainfall data time series for a specific site and GCM projections have different patterns and temporal resolutions. The site-specific rainfall data time series shown in Figure 1(a) is defined as $\boldsymbol{f}_1$, which is often available at an hourly interval. $\boldsymbol{f}_1$ includes both past observation records and future projections to be obtained from the proposed method. Note that the future projection at a specific site is not known currently, but the intended outcome of the proposed method and the required input for many climate change-related engineering applications. The GCM rainfall projection shown in Figure 1(b) is defined as $\boldsymbol{f}_2$ with a relatively low temporal resolution (e.g. monthly), including both historical simulation results and scenario-based projections for the future. Generally speaking, high-temporal-resolution data (e.g. hourly rainfall data time series) is highly variable and inherently stochastic, characterised by a high proportion of dry hours interspersed with occasional heavy rain events. Such characteristics result in highly skewed and heavy – tailed distributions, as illustrated by $\boldsymbol{f}_1$ in Figure 1(a), posing significant challenges to data analysis. On the other hand, an aggregation of the hourly rainfall data time series to a monthly scale (for example, see $\boldsymbol{f}_2$ in Figure 1(b)), smooths out high – frequency variability while preserving key low – frequency structures such as seasonality, interannual variability, long-term trends and localised bursts. Because of these structured characteristics, the monthly rainfall data time series can be sparsely represented by only a limited number of basis functions after a suitable transformation (Peleg, Eldar, and Elad 2012), a method often used in big data analytics and machine learning (Sandryhaila and Moura 2014; Wright et al. 2010; Zhang et al. 2015). In addition, note that the site-specific rainfall pattern $\boldsymbol{f}_1$ and the regional GCMs rainfall projection $\boldsymbol{f}_2$ are correlated. They therefore share some common features but also retain individual characteristics (Deng et al. 2013; Duarte et al. 2008; Elad and Aharon 2006; Guan and Wang 2024). Therefore, they may be jointly modelled under a JSR framework, as shown in Figure 3. Using JSR to jointly represent $\boldsymbol{f}_1$ and $\boldsymbol{f}_2$ for site-specific projection of future rainfall patterns ensures that these site-specific projections not only align with the regional trend of climate change predicted by GCMs, but also incorporate localised rainfall characteristics observed from past rainfall records at a specific site.

Note that the projected results under the JSR framework have a relatively low temporal resolution (e.g. monthly), which is insufficient for many engineering applications. Therefore, temporal downscaling is performed on the site-specific projection of rainfall patterns obtained from JSR, using a stochastic storm selection method (Socolofsky et al. 2001; Takhellambam et al. 2022). This method has the advantage of only

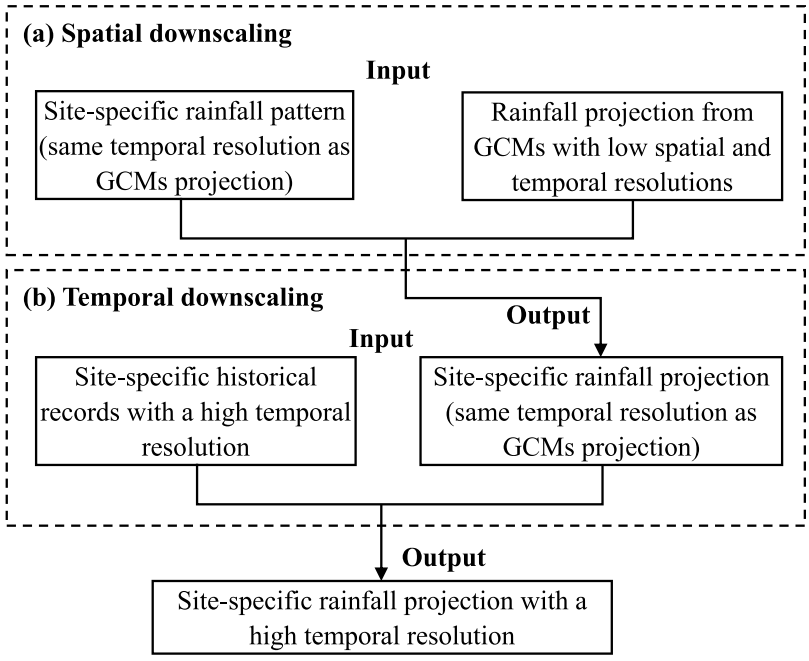

Figure 2. The proposed two-step framework for spatial and temporal downscaling.

requiring a small number of model parameters. It stochastically selects and assembles historical rainfall events so that the temporally downscaled time series with a high temporal resolution (e.g. hourly) matches the low-temporal-resolution totals while preserving realistic event characteristics. Details of the JSR for spatial downscaling and stochastic storm selection for temporal downscaling are provided in the following two sections, respectively.

3. Spatial downscaling for site-specific rainfall patterns under the JSR framework

3.1. Joint sparse representation of rainfall data time series

Fourier series expansion is a powerful mathematical tool for representing continuous functions (Stein and Shakarchi 2003). As shown in Equation (1), it expresses a continuous function as an infinite sum of orthogonal sine and cosine basis functions, each corresponding to a specific frequency:

$$f(t) = \frac{a_0}{2} + \sum_{n=1}^{\infty}\left[a_n \cos\left(\frac{2\pi nt}{T}\right) + b_n \sin\left(\frac{2\pi nt}{T}\right)\right] \quad (1)$$

where $f(t)$ is a function of interest (e.g. a rainfall data time series in Figure 1); a_0 is the average component of $f(t)$ over one period; a_n and b_n, $n = 0, 1, \ldots, \infty$, are the coefficients, representing the amplitude (or weight) of each frequency component for the function; T is the fundamental period of $f(t)$. It has been analytically proved that any square-integrable function in the L^2 space can be represented by such a Fourier series (Edwards 1982; Stein and Shakarchi 2003). This theoretical foundation ensures that a wide range of real-world data or signals, including time series signals (e.g. rainfall data time series), can be effectively decomposed into simple oscillatory components. Each component reveals distinct frequency behaviour, allowing complex signals to be interpreted through their spectral structure in the frequency domain. This naturally motivates a transformation from a time domain into a frequency domain, where patterns such as trends, periodicities and noise can be clearly identified, quantified and separated (Oppenheim 1999; Rashid, Beecham, and Chowdhury 2015; van den Enden and Verhoeckx 1989; Wallace and Dickinson 1972). This principle underpins numerous applications, such as in signal processing (Sandryhaila and Moura 2014; Stankovic et al. 2019; Wright et al. 2010; Zhang et al. 2015), heat conduction (Narasimhan 1999), geophysics (Bath 2012; Wang, Hu, and Phoon 2022), as well as climate data analysis (Laguardia 2011; Nerini et al. 2017; Yiou, Baert, and Loutre 1996).

In addition, natural signals (e.g. rainfall data time series) often exhibit inherent structural patterns. In other words, their essential features can be captured by just a few dominant frequency components. With a suitable transformation, such as the Fourier transform (Oppenheim 1999), wavelet transform (Daubechies 1992; Mallat 1999), or discrete cosine transform (DCT) (Ahmed, Natarajan, and Rao 1974; Rao and

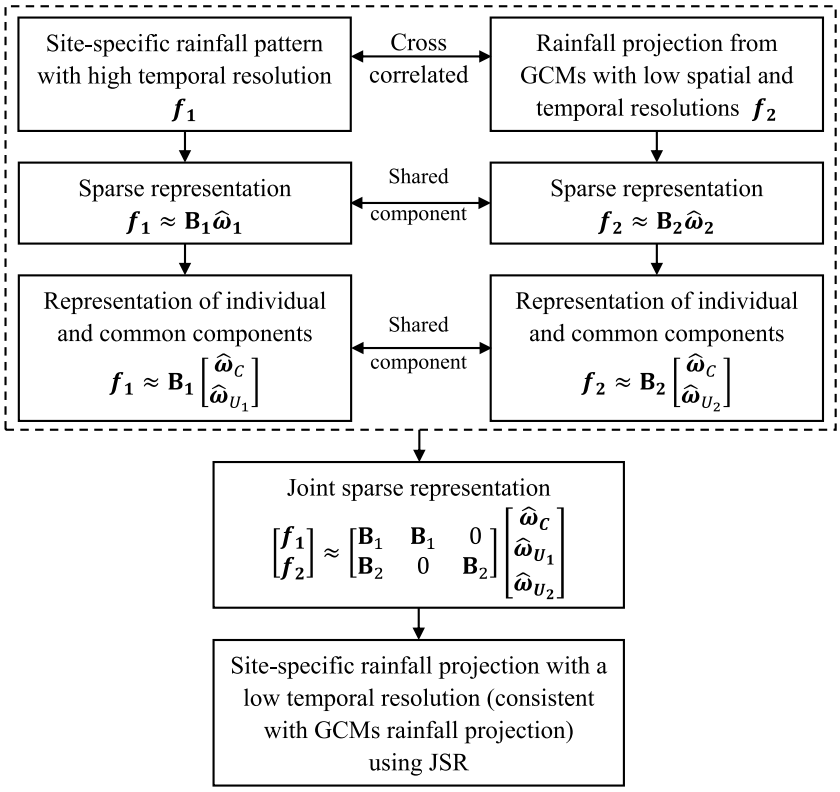

Figure 3. The proposed joint sparse representation (JSR) framework for site-specific rainfall projection contributed by climate change.

Yip 2014; Strang 1999), most of the coefficients are either zero or negligibly small. This phenomenon is referred to as data sparsity or compressibility, which allows a signal to be efficiently represented by only a limited number of basis vectors selected from a properly predefined dictionary (Candès and Wakin 2008; Donoho 2006). Under this sparse representation, a signal $\boldsymbol{f}$ can be accurately approximated using a linear combination of basis vectors or functions, as shown in Equation (2) (Candès, Romberg, and Tao 2006; Elad 2010; Fornasier and Rauhut 2015; Mallat 1999; Peleg, Eldar, and Elad 2012).

$$\boldsymbol{f} \approx \mathbf{B}\hat{\boldsymbol{\omega}} \tag{2}$$

where $\mathbf{B}$ is an $N \times N$ orthonormal matrix and its element $B(i, j)$ denotes the value of the ith basis function evaluated at the jth position; $\hat{\boldsymbol{\omega}}$ is the sparse weight coefficient estimated. Consider, for example, the monthly rainfall records from rain gauge N05 in Hong Kong (see Figure 1) and data transformation by DCT. To construct DCT basis functions, Equation (3) below is adopted to calculate $B(i, j)$. DCT has proven effectiveness in compactly representing signals with strong periodic or quasi-periodic components (Ahmed, Natarajan, and Rao 1974; Strang 1999). Additionally, it can be efficiently implemented using built-in functions available in many computing environments, such as MATLAB or Python (e.g. dctmtx in MATLAB, scipy.fftpack in Python).

$$B(i,j) = \begin{cases} \dfrac{1}{\sqrt{N}} & \text{for } j = 1, i = 1, 2, \ldots, N \\ \sqrt{\dfrac{2}{N}}\cos\dfrac{\pi(j-1)(2i-1)}{2N} & \text{for } j = 2, \ldots, N, i = 1, 2, \ldots, N \end{cases} \tag{3}$$

After applying DCT transformation (e.g. dctmtx in MATLAB) to monthly rainfall records at rain gauge N05, the obtained weight coefficients are shown in Figure 4(a). The values of weight coefficients decay rapidly and only a few weight coefficients have a significant magnitude. Then, the rainfall data time series can be effectively reconstructed using a limited number of important basis functions with significant weight coefficients. For example, a reconstruction using the top 30% of DCT coefficients with the largest absolute values can achieve a relative reconstruction error as low as 3.4% when compared with the original rainfall data, as shown Figure 4(b). This indicates that the dominant basis functions are sufficient to capture the main features of the rainfall data time series. This sparse representation of rainfall data time series has been observed at many rain gauge stations.

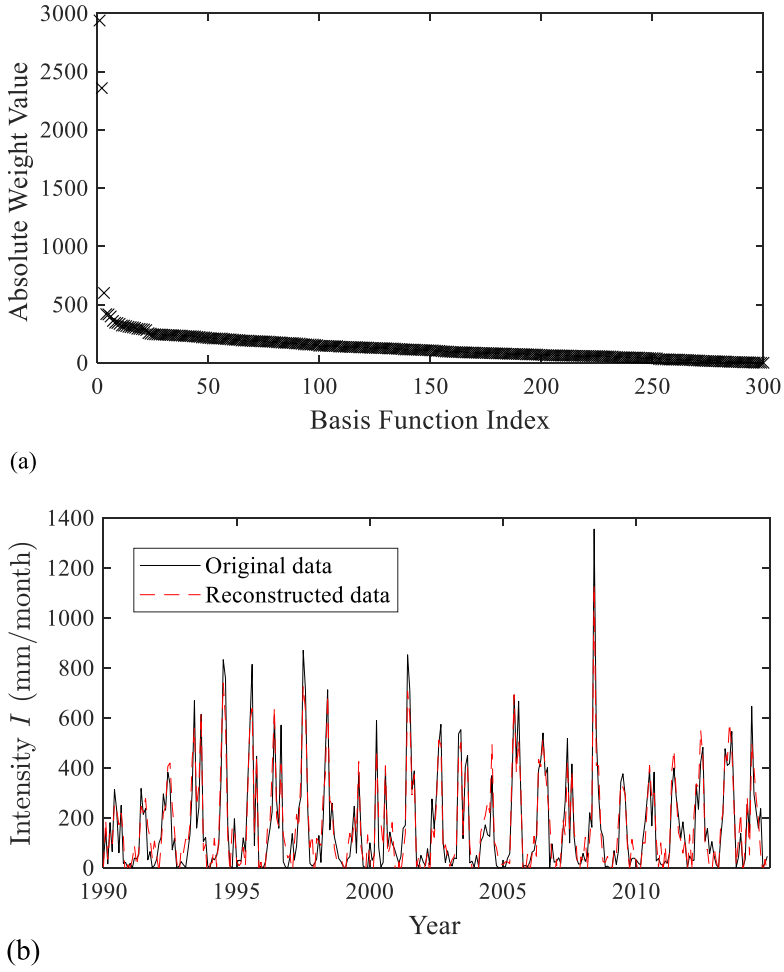

Figure 4. An illustration of the sparse representation of rainfall data time series (a) Rank of the coefficient weight absolute value (b) Comparison of the original rainfall data time series and those reconstructed using the top 30% of the weight coefficients.

In addition to the sparse representation of rainfall data time series (e.g. $\boldsymbol{f}_1$ and $\boldsymbol{f}_2$ in Figure 1), rainfall patterns at specific sites and those over the region where the sites are located often exhibit a positive correlation (Maraun et al. 2010). The site-specific rainfall pattern is not only influenced by large-scale atmospheric processes, but also exhibits unique localised variability. Consequently, site-specific rainfall patterns and GCM rainfall projections in the corresponding area are expected to share a similar trend of overall change, but also contain their respective individual patterns. Under a JSR framework (see Figure 3), $\boldsymbol{f}_1$ and $\boldsymbol{f}_2$ can be treated as a summation of the common components, denoted as $\boldsymbol{f}_C$ and their individual patterns, denoted as $\boldsymbol{f}_{U_i}$ (e.g. Baron et al. 2006).

$$\boldsymbol{f}_i = \boldsymbol{f}_C + \boldsymbol{f}_{U_i} \approx \mathbf{B}_i \hat{\boldsymbol{\omega}}_C + \mathbf{B}_i \hat{\boldsymbol{\omega}}_{U_i} \tag{4}$$

where $\mathbf{B}_i$ is the basis function matrix; $\hat{\boldsymbol{\omega}}_C$ and $\hat{\boldsymbol{\omega}}_{U_i}$ are the weight coefficients for the common and individual components, respectively. JSR is designed to handle an ensemble of signals by jointly representing them over a shared set of basis functions, while allowing for both common and individual components across signals (Duarte and Eldar 2011). It leverages cross-correlation among signals, leading to more efficient representations and improved robustness to noise and missing data (e.g. missing projection of future rainfall pattern at specific sites in this study, as shown in Figure 1(a)). This makes JSR widely applicable in various fields, such as image compression and signal processing (Deng et al. 2013; Duarte et al. 2008; Elad and Aharon 2006). Leveraging this relationship in the proposed method, JSR is used to jointly model the ensemble, enabling enhanced projection of rainfall patterns at specific sites under climate change. Let $\boldsymbol{f}$ denote a matrix composed of both time series data $\boldsymbol{f}_1$ and $\boldsymbol{f}_2$, which are assembled into a single matrix, as shown in Equation (5), under the JSR framework.

$$\boldsymbol{f} = \begin{bmatrix} \boldsymbol{f}_1 \\ \boldsymbol{f}_2 \end{bmatrix} \approx \mathbf{B}^e \boldsymbol{\omega}^e \approx \begin{bmatrix} \mathbf{B}_1 & \mathbf{B}_1 & \mathbf{0} \\ \mathbf{B}_2 & \mathbf{0} & \mathbf{B}_2 \end{bmatrix} \begin{bmatrix} \boldsymbol{\omega}_C \\ \boldsymbol{\omega}_{U_1} \\ \boldsymbol{\omega}_{U_2} \end{bmatrix} \tag{5}$$

where $\mathbf{B}^e$ is the joint basis function; $\hat{\boldsymbol{\omega}}^e$ is the ensembled weight. Equation (5) ensures a coherent selection of basis functions that applies to both time series of $\boldsymbol{f}_1$ and $\boldsymbol{f}_2$, leading to better alignment and fusion of both site-specific and GCMs projection time series. Therefore, JSR preserves the local variability while maintaining consistency with overall climate change patterns in the region.

3.2. Site-specific rainfall projection under JSR framework

As defined in Section 2, $\boldsymbol{f}_1$ and $\boldsymbol{f}_2$, with N time steps, represent the rainfall data time series from the past to the future. However, future projections are missing for $\boldsymbol{f}_1$, the rainfall pattern at a specific site, as shown in Figure 1(a). M denotes the number of available observation data points from the past at a specific site, where $M < N$ and the measured rainfall records at a specific site are denoted by a vector $\boldsymbol{y}_1$with a length of M. Similarly, $\boldsymbol{y}_2$ represents the available rainfall data time series from GCMs with N time steps (i.e. all N time steps have projection results from GCMs). To relate the available records to the full rainfall data time series $\boldsymbol{f}_i$, $i = 1$ or 2, a binary sensing matrix $\boldsymbol{\psi}_\mathbf{i}$ is constructed to indicate the positions of available measurements.

$$\boldsymbol{y}_i = \boldsymbol{\psi}_i \boldsymbol{f}_i \approx \boldsymbol{\psi}_i \mathbf{B}_\mathbf{i} \hat{\boldsymbol{\omega}}_C + \boldsymbol{\psi}_i \mathbf{B}_\mathbf{i} \hat{\boldsymbol{\omega}}_{U_i} \approx \mathbf{A}_i \hat{\boldsymbol{\omega}}_C + \mathbf{A}_i \hat{\boldsymbol{\omega}}_{U_i} \quad (6)$$

The matrix $\boldsymbol{\psi}_1$ has a dimension of $M \times N$ and it is used to extract the first M time steps from the full signal $\boldsymbol{f}_1$, corresponding to the available measurements (i.e. rainfall historical records at a specific site). $\boldsymbol{\psi}_2$ is an identity matrix with a dimension of $N \times N$, indicating that the full time series can be obtained from GCM projections $\boldsymbol{f}_2$. $\mathbf{A}_i = \boldsymbol{\psi}_i \mathbf{B}_\mathbf{i}$ is the measurement matrix. Therefore, the available rainfall data time series ensemble $\boldsymbol{y}^e$, including site-specific rainfall records $\boldsymbol{y}_1$ and available GCMs' projection of the rainfall data time series $\boldsymbol{y}_2$, can be expressed as follows:

$$\boldsymbol{y}^e = \begin{bmatrix} \boldsymbol{y}_1 \\ \boldsymbol{y}_2 \end{bmatrix} \approx \mathbf{A}^e \hat{\boldsymbol{\omega}}^e \approx \begin{bmatrix} \mathbf{A_1} & \mathbf{A_1} & \mathbf{0} \\ \mathbf{A_2} & \mathbf{0} & \mathbf{A_2} \end{bmatrix} \begin{bmatrix} \hat{\boldsymbol{\omega}}_\mathbf{C} \\ \hat{\boldsymbol{\omega}}_{\mathbf{U}_1} \\ \hat{\boldsymbol{\omega}}_{\mathbf{U}_2} \end{bmatrix} \quad (7)$$

where $\mathbf{A}^e$ is a joint measurement matrix. Since the records at a specific site only include the past M time steps, the missing measurements cause inevitable uncertainties when estimating $\hat{\boldsymbol{\omega}}^e$ to reconstruct the complete rainfall time series $\boldsymbol{f}_1$. To approximate the $\hat{\boldsymbol{\omega}}^e$ using only available measurements and quantify the uncertainties, a Bayesian framework is adopted (Guan, Wang, and Phoon 2024; Ji, Xue, and Carin 2008; Tipping 2001).

$$p(\hat{\boldsymbol{\omega}}^e | \boldsymbol{y}^e) = \frac{p(\boldsymbol{y}^e | \hat{\boldsymbol{\omega}}^e) \times p(\hat{\boldsymbol{\omega}}^e)}{p(\boldsymbol{y}^e)} \quad (8)$$

where $p(\hat{\boldsymbol{\omega}}^e | \boldsymbol{y}^e)$ represents the posterior probability distribution of $\hat{\boldsymbol{\omega}}^e$ given $\boldsymbol{y}^e$; $p(\hat{\boldsymbol{\omega}}^e)$ is the prior distribution; $p(\boldsymbol{y}^e)$ is the evidence, ensuring a normalising constant to maintain the valid distribution; $p(\boldsymbol{y}^e | \hat{\boldsymbol{\omega}}^e)$ is the likelihood function.

A zero-mean Gaussian measurement error with an unknown variance σ^2 is adopted for each observation and the corresponding likelihood function that accounts for these uncertainties is formulated as (e.g. Tipping 2001).

$$p(\boldsymbol{y}^e | \hat{\boldsymbol{\omega}}^e) = \frac{1}{(2\pi\sigma^2)^{m/2}} \exp\left(-\frac{1}{2\sigma^2} \parallel \boldsymbol{y}^e - \mathbf{A}^e \hat{\boldsymbol{\omega}}^e \parallel^2 \right) \quad (9)$$

where m is the number of data points; $\boldsymbol{y}^e - \mathbf{A}^e \hat{\boldsymbol{\omega}}^e$ is the residual; σ^2 is modelled as an unknown parameter equalling to unknown variance $1/\tau$. To promote the sparse solutions, a hierarchical prior is employed with a three-level Gaussian-inverse Gamma-Gamma prior shown by Equation (10) and its specific terms described in Equations (11) to (14), respectively (Guan, Wang, and Phoon 2024; Zhao and Wang 2020).

$$p(\hat{\boldsymbol{\omega}}^e, \boldsymbol{\alpha}, \gamma, \tau) = p(\hat{\boldsymbol{\omega}}^e | \boldsymbol{\alpha}) p(\boldsymbol{\alpha} | \gamma) p(\gamma) p(\tau) \quad (10)$$

$$p(\hat{\boldsymbol{\omega}}^e | \boldsymbol{\alpha}) = \prod_{t=1}^{N_t} \alpha_t^{1/2} (2\pi)^{-1/2} \exp[-\alpha_t (\hat{\omega}_t^e)^2 / 2] \quad (11)$$

$$p(\boldsymbol{\alpha} | \gamma) = \prod_{t=1}^{N_t} \frac{\gamma}{2} \alpha_t^{-2} \exp\left(-\frac{\gamma}{2} \alpha_t^{-1} \right) \quad (12)$$

$$p(\gamma) = \frac{(b_0)^{a_0} \gamma^{a_0 - 1}}{\Gamma(a_0)} \exp(-b_0 \gamma) \quad (13)$$

$$p(\tau) = \frac{(d_0)^{c_0} \tau^{c_0 - 1}}{\Gamma(c_0)} \exp(-d_0 \tau) \quad (14)$$

where the first level $p(\hat{\boldsymbol{\omega}}^e | \boldsymbol{\alpha})$ in Equation (11) assumes that $\hat{\boldsymbol{\omega}}^e$ follow a Gaussian distribution, encouraging most weights to be close to 0 while allowing for the possibility of large weights. $\boldsymbol{\alpha}$ controls the variability of $\hat{\boldsymbol{\omega}}^e$, determining the level of spread for the weight values. The second level, as expressed in Equation (12), uses an inverse gamma distribution, capturing the uncertainty and allowing flexibility in variance. The hyperparameter, γ, related to the variance $\boldsymbol{\alpha}$ in Equation (13) is modelled as a gamma distribution, which ensures that the variability of $\boldsymbol{\alpha}$ is modelled. In

addition, the regularisation parameter τ in Equation (14) following a gamma prior is introduced to control the overall sparsity and smoothness of the estimated weights. a_0, b_0, c_0, d_0 are non-negative constants.

Since no analytical solution is available for the posterior probability distribution, Gibbs sampling is adopted for inference (Casella and George 1992; Robert 2014). The process begins by initialising hyperparameters and parameters and computing matrices. Specifically, a sampling strategy is employed to sequentially update parameters, where each parameter is sampled from its corresponding conditional distribution while using the most recent updates of the others. Once convergence is achieved, posterior samples of $\hat{\boldsymbol{\omega}}^{e}$ are used to reconstruct the full time series, as described in Equation (5). The details of the Gibbs sampling process follow the approach of Guan, Wang, and Phoon (2024). Figure 5 shows a flowchart for JSR-based Bayesian inference using Gibbs sampling. The posterior mean of the reconstructed time series is calculated as the average across all $\hat{\boldsymbol{\omega}}^{e}$ samples, which can be used as the projection results for engineering design and decision-making, as it reflects a statistically consistent estimate of the temporal trend. The uncertainty can also be quantified by the standard deviation of these samples at each time step.

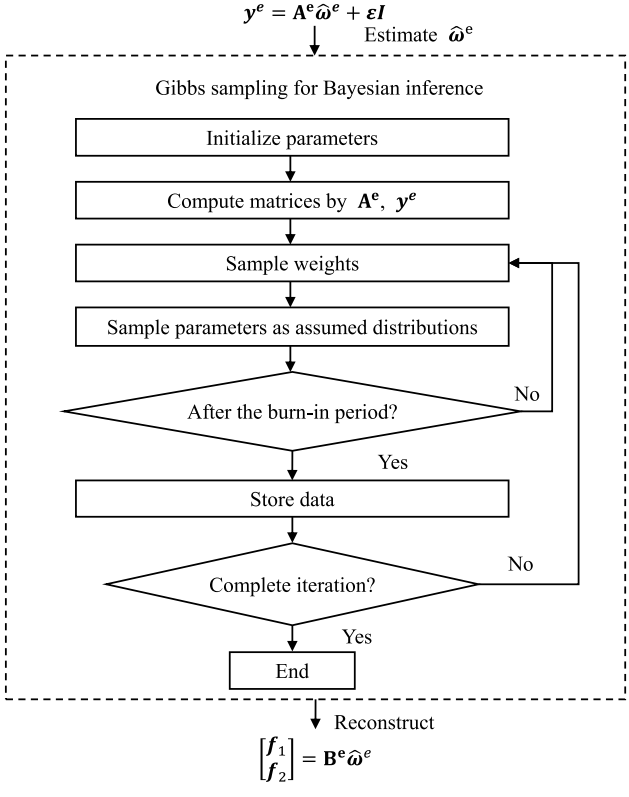

Figure 5. Process of Bayesian inference to estimate $\hat{\boldsymbol{\omega}}^{e}$ and $\boldsymbol{f}_i$.

4. Temporal downscaling of site-specific rainfall projection results

The site-specific projection results have a low temporal resolution (e.g. monthly), making temporal downscaling necessary for engineering applications. In this study, a stochastic storm selection method is adopted (Socolofsky, Adams, and Entekhabi 2001; Takhellambam et al. 2022), which is computationally efficient and requires only a few parameters. Figure 6 illustrates the idea of the stochastic storm selection method, which downscales site-specific monthly projection results into hourly rainfall events. First, historical hourly rainfall records at the projection site are arranged as a sequence of discrete rainfall events. Then, the total rainfall amount of each discrete event is calculated and the total rainfall amounts of all discrete events are used to construct an empirical cumulative distribution function (CDF) that guides the stochastic process of storm selection. In this process, random numbers are repeatedly drawn from a uniform distribution and their corresponding quantiles on the empirical CDF determine the rainfall amounts of the selected events. The temporal profiles of these events are inherited from the historical records, which provide the observed hourly intensity patterns and durations for each event. For example, when downscaling a monthly rainfall projection, historical events are sequentially sampled by drawing uniform random numbers between 0 and the cumulative probability corresponding to the remaining monthly rainfall to be allocated. A small tolerance threshold is pre-set to define an acceptable difference between the cumulative rainfall of the selected events and the target monthly total. The selection procedure is repeated until the value of the difference is smaller than this threshold ε. For each selected event, the duration and hourly intensity are derived from the historical events that are used to determine its total rainfall. The resulting hourly rainfall events are thus consistent with both the low-temporal-resolution projection at the specific site and the statistical characteristics of historical events observed at the same site. In stochastic storm selection, a critical factor influencing the temporal downscaling results is the definition of a rainfall event. For example, when the output is intended for slope stability analysis, as illustrated in Figure 7, hourly rainfall events are needed and might be defined as continuous rainfall periods separated by at least 9 dry hours (Joo et al. 2014; Jun et al. 2017). Such a definition excludes minor rainfall between major events and avoids misclassification.

Figure 8 illustrates a flowchart of the detailed procedure. The process begins with the definition and summarisation of historical rainfall events at the target specific site, where hourly rainfall records are

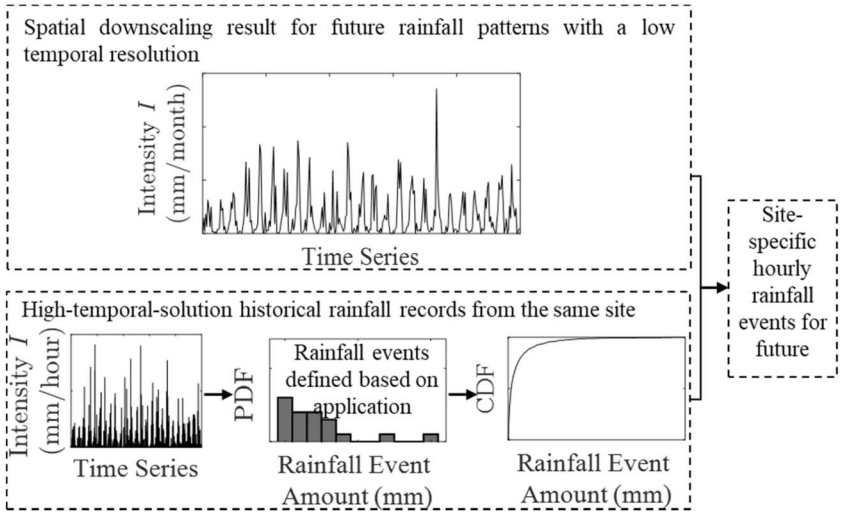

Figure 6. Illustration of stochastic storm selection for temporal downscaling.

segmented into discrete rainfall events based on a predefined criterion. For each rainfall event, the total rainfall amount is calculated and these totals are then used to construct a CDF. Given a monthly target rainfall amount D_t, the method searches the CDF to determine the cumulative probability a, associated with the current D_t. A uniform random number u is then drawn between 0 and a and the corresponding historical event with rainfall amount D_i is selected. The residual target is subsequently updated as $D_t - D_i$ and this process is repeated until the residual is smaller than a predefined tolerance threshold ε. Each selected event is assigned the same duration and intensity as its corresponding historical event, ensuring that the generated hourly rainfall events preserve realistic temporal characteristics.

5. Implementation procedure

The implementation procedure of the proposed site-specific projection method, including spatial and temporal downscaling, is summarised below and illustrated in Figure 9. The proposed method uses site-specific rainfall records and the GCM projections at the grid cell covering the site of interest. The procedure consists of six steps, with the details of each step summarised as follows:

Step 1: Collect the available site-specific rainfall records $\boldsymbol{y}_1$ and the GCM monthly rainfall projection $\boldsymbol{y}_2$, aggregate the site-specific rainfall records to match the GCM temporal resolution.

Step 2: Construct the basis function $\mathbf{B_i}$ using DCT and representing the measurements in the frequency domain, as shown in Equation (6).

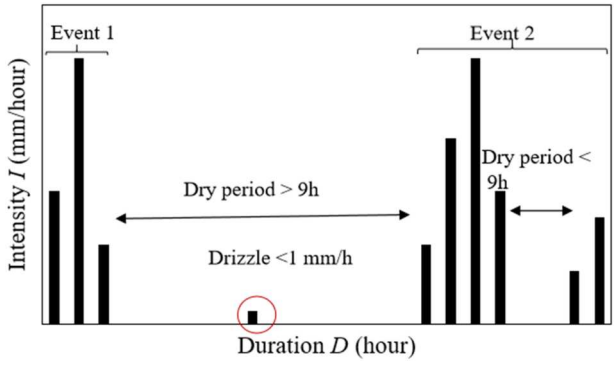

Figure 7. Illustration of rainfall event definition for slope stability design.

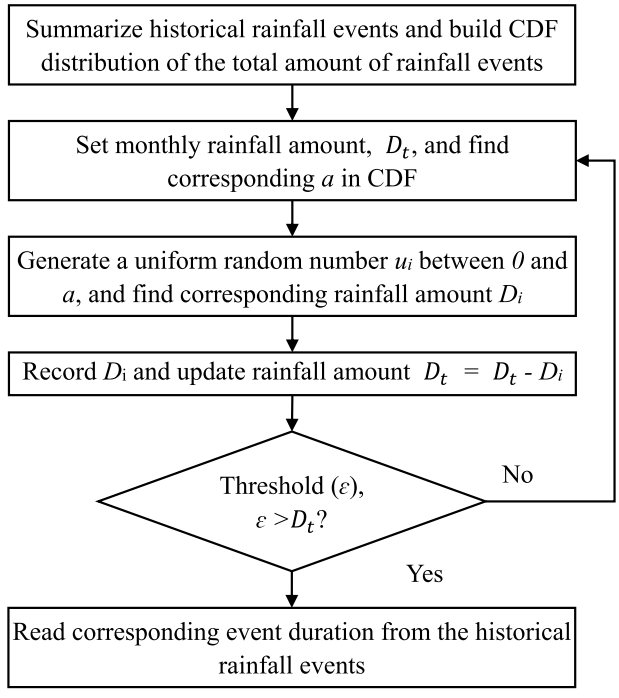

Figure 8. A flowchart of the stochastic storm selection method (after Socolofsky, Adams, and Entekhabi 2001).

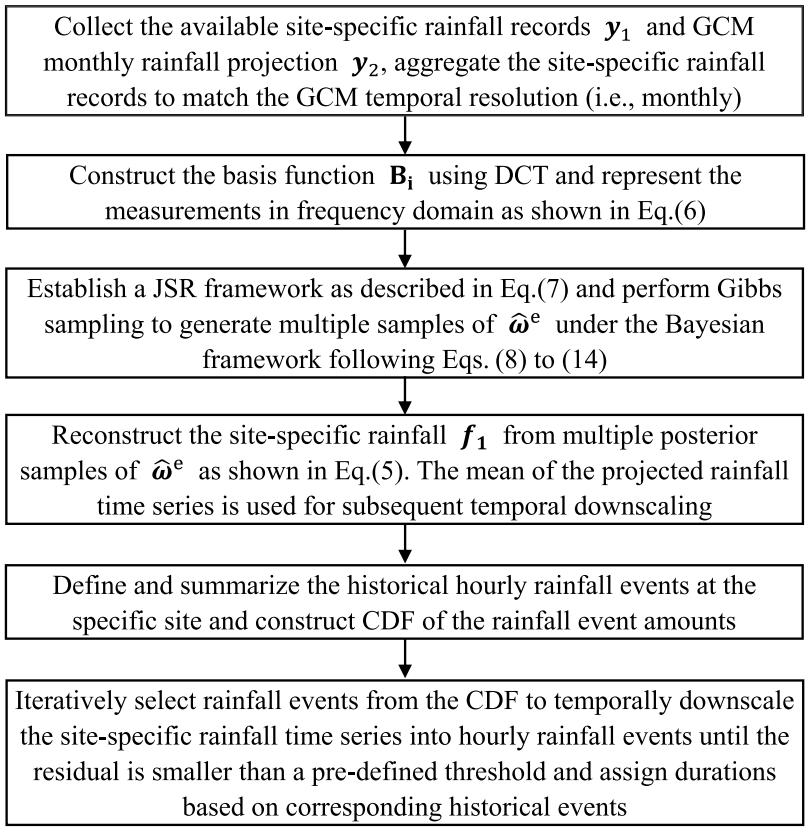

Figure 9. Implementation procedure of the proposed method.

Step 3: Establish a JSR framework as described in Equation (7) and perform Gibbs sampling to generate multiple samples of $\hat{\omega}^e$ under the Bayesian framework, following Equations (8) to (14).

Step 4: Reconstruct the site-specific rainfall f_1 from multiple posterior samples of $\hat{\omega}^e$ as shown in Equation (5). The mean of the projected rainfall data time series is used for subsequent temporal downscaling.

Step 5: Define and summarise the historical hourly rainfall events at the specific site and construct a CDF of the rainfall event amounts.

Step 6: Iteratively select rainfall events from the CDF to temporally downscale the site-specific rainfall data time series into hourly rainfall events until the residual is smaller than a pre-defined threshold and assign durations based on corresponding historical events.

6. Illustrative example

6.1. Site-specific and model rainfall data time series

To demonstrate the proposed method, an illustrative example is presented using a site-specific rainfall record and GCM rainfall projection. The site-specific rainfall data time series is from rain gauge N05 in the New Territories, Hong Kong. It provides complete and reliable hourly rainfall records from January 1990 to December 2014, as shown in Figure 10(a). The hourly rainfall pattern is characterised by a high proportion of zero values (93.46%), while occasional extreme events can reach high intensities (e.g. 81.5 mm/h recorded in June 2008). Statistical analysis using Equations (15) and (16) yield a coefficient of variation (CV) of 3.41 and a skewness of 6.93, indicating a highly skewed and heavy-tailed distribution.

$$CV = \frac{\sigma}{\mu} \tag{15}$$

$$\text{Skewness} = \frac{n}{(n-1)(n-2)} \sum_{i=1}^{n} \left(\frac{x_i - \mu}{\sigma} \right)^3 \tag{16}$$

where σ is the standard deviation and μ is the mean. For implementation, the hourly rainfall is aggregated into monthly totals to facilitate a sparse representation. Figure 10(b) shows the monthly rainfall data time series, with a mean of 188.8 mm, a standard deviation of 214.0 mm, a CV of 1.16 and a skewness of 1.87. It exhibits strong seasonality and interannual variability, characterised by alternating dry and wet years. Most

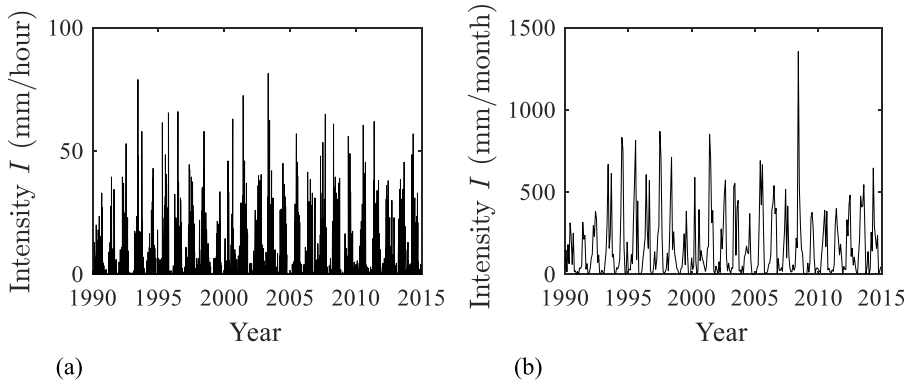

Figure 10. Rainfall data time series at N05 rain gauge (January 1990–December 2014) (a) Hourly rainfall data time series (b) Monthly rainfall data time series.

rainfall occurs during the summer months, often in the form of intense storms.

In addition to the site-specific rainfall record, monthly rainfall projections are obtained from the ACCESS-CM2 model (Australian Community Climate and Earth-System Simulator, Climate Model Version 2), which are publicly available through the Earth System Grid Federation (ESGF) and other climate data repositories. The selected model is used to illustrate the proposed framework, which can be readily applied to projections from other climate models. In this study, the grid cell containing N05 rain gauge is extracted from the model outputs, producing rainfall data time series of historical simulation from January 1990 to December 2014, and scenario – based projection from January 2015 to December 2064 under the low – emission pathway SSP1-2.6, as shown in Figure 11. For the historical period, the mean monthly rainfall is 216.0 mm with a standard deviation of 155.7 mm and a CV of 0.72. For the future, the mean monthly rainfall is 221.8 mm, with a standard deviation of 176.9 mm and a CV of 0.80.

Two cases are projected in this illustrative example using the proposed method. The first case is to project the site – specific monthly rainfall series at N05 during 2010–2014 using the monthly rainfall series at rain gauge N05 during 1990–2009 ($\boldsymbol{y}_1$) and the GCM rainfall projection during 1990–2014 ($\boldsymbol{y}_2$) as inputs under the JSR framework. The spatially downscaled monthly result is subsequently temporally downscaled, based on a CDF derived from historical hourly events at N05 during 1990–2009. Figure 12 shows the histogram of historical hourly rainfall event amounts and the corresponding CDF. In the first case, the projected results will be compared with real observations at N05 during 2010–2014. In the second case, the rainfall patterns at N05 during 2015–2064 under the low-emission scenario SSP1-2.6 are projected using GCM monthly rainfall output during 1990–2064 together with the historical rainfall record at N05 during 1990–2014.

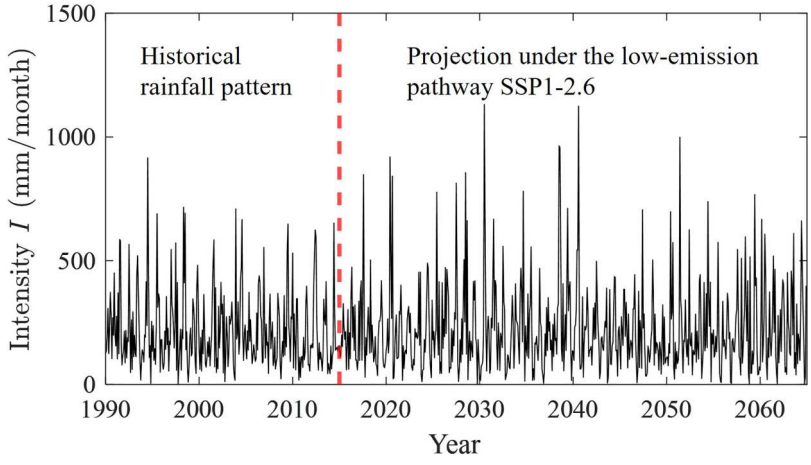

Figure 11. Monthly rainfall data time series simulated by ACCESS-CM2 for the region where N05 rain gauge is located (January 1990–December 2064).

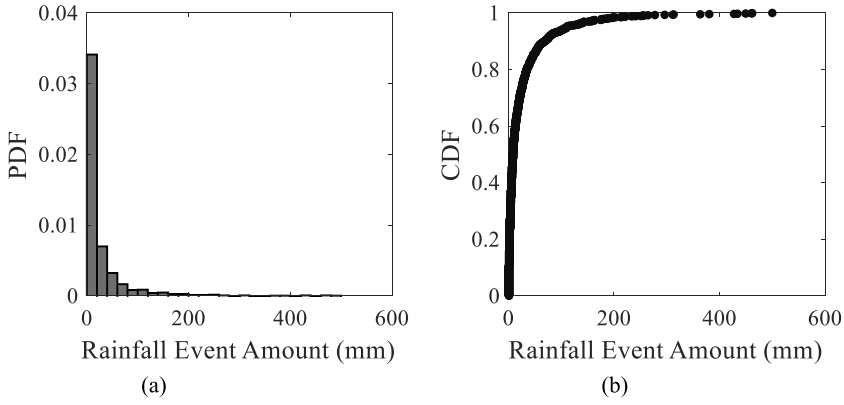

Figure 12. Probability distribution of hourly rainfall event amount at N05 rain gauge (January 1990–December 2009) (a) Histogram (b) CDF.

6.2. Spatial downscaling results and validation (Case 1)

6.2.1. JSR results

In this section, the proposed JSR method is applied to generate 200 monthly rainfall projection samples at N05 for Case 1. Figure 13 shows typical wet and dry samples generated, along with the observed monthly rainfall record at N05 during 2010–2014. The wet sample represents a generated rainfall sequence whose total rainfall over the considered period is significantly higher than the mean total rainfall of all generated sequences. In contrast, the dry sample represents a generated rainfall sequence whose total rainfall over the considered period is lower than the mean total rainfall of all generated sequences. Figure 13(a) shows their time series, capturing the seasonal variations that largely agree with the observations despite differences in magnitude. Figure 13(b) shows their CDFs for comparing the overall distribution of intensity. The dry sample's CDF is consistently shifted towards smaller values, while the wet sample exhibits a heavier tail, indicating more frequent high-intensity monthly rainfall. This spread reflects the inherent uncertainty, which may stem from the limited information, including site-specific historical rainfall and large-scale GCM trends and the randomness of rainfall. The proposed JSR method captures this uncertainty by generating a plausible range of rainfall scenarios, from conservative low-rainfall conditions to wet conditions, instead of providing a single deterministic result.

6.2.2. Validation of spatial downscaling results

This section presents a quantitative evaluation of the spatial downscaling results. Several statistical indicators, including the μ, σ and CV, are computed by comparing the mean projection of the 200 posterior samples with the real observation during 2010–2014. Figure 14(a) illustrates the mean projection rainfall data time series alongside the observed monthly rainfall data time series during 2010–2014. Quantitatively, the average monthly rainfall is 166.5 mm from observation and 155.0 mm from the mean projection in Figure 14(a), resulting in

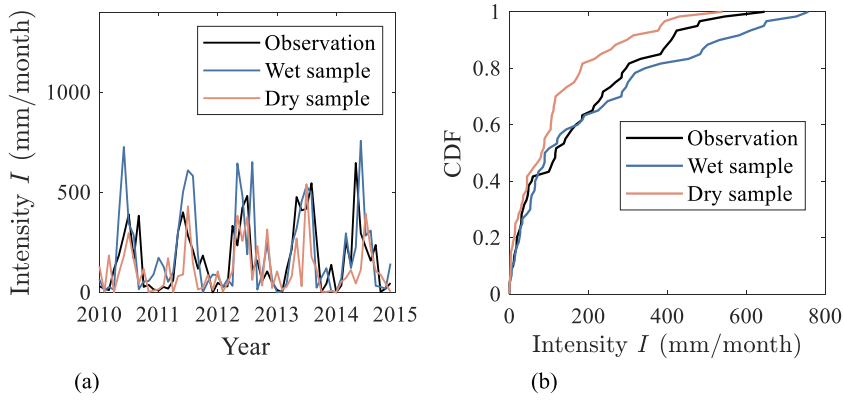

Figure 13. Comparison of spatially downscaled wet and dry rainfall projection samples with observation at N05 rain gauge (January 2010–December 2014) (a) Comparison of time series (b) Comparison of CDF.

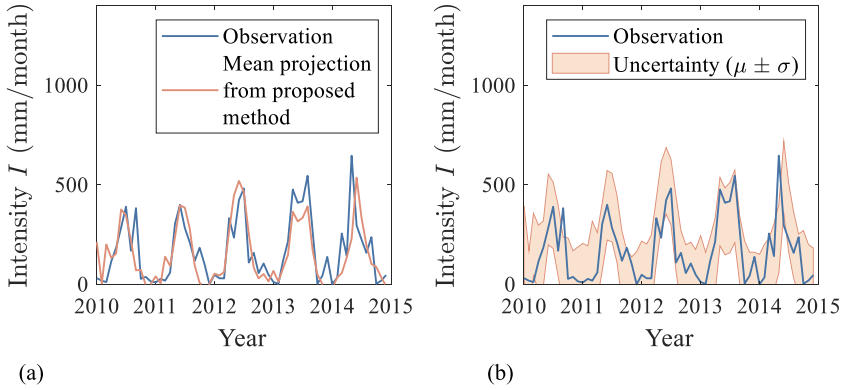

Figure 14. Validation of spatially downscaled rainfall projections from the proposed method against observation at N05 rain gauge (January 2010–December 2014) (a) Comparison between mean projection and observation (b) Uncertainty in projections and observation.

a relative difference of 6.9%. The standard deviation is also closely matched as 161.5 mm from observations and 151.5 mm from the projection, with a relative difference of 6.2%. The CV is exactly 1.0 for both observation and mean projection. This suggests that the model captures the overall tendency and reflects the characteristics of rainfall variation. In addition, Figure 14(b) shows the uncertainty band ($\mu \pm 1\sigma$) of the projected results and the observation generally falls within the uncertainty band. It demonstrates that the proposed JSR method provides a reliable envelope for the site-specific rainfall pattern.

To further evaluate the agreement in overall distribution, Figure 15 compares CDFs of the mean projection and observation. To evaluate the overall distribution of rainfall and statistical structure of the entire time series, a two-sample Kolmogorov–Smirnov (K–S) test (Justel, Peña, and Zamar 1997) is performed to assess whether two samples come from the same distribution by comparing their CDFs. The test statistics

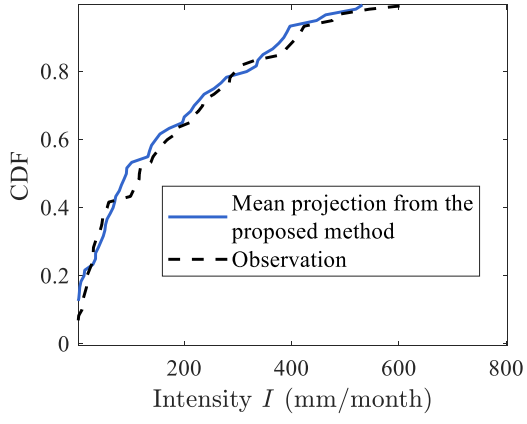

Figure 15. Comparison of CDFs between the spatial downscaled mean projection from the proposed method and observation at N05 rain gauge (January 2010–December 2014).

are defined as follows:

$$D = \max_{x} |F_X(x) - F_Y(x)| \tag{17}$$

$$D_{\text{critical}} = 1.36 \cdot \sqrt{\frac{n_1 + n_2}{n_1 \cdot n_2}}, \text{ for significance level at 0.05} \tag{18}$$

where $F_X(x)$ and $F_Y(x)$ are empirical CDFs of samples X and Y, respectively; D is the maximum absolute difference between $F_X(x)$ and $F_Y(x)$; D_{critical} is a critical value; $n_1$and n_2 are the sample sizes of X and Y, respectively. If D is smaller than D_{critical}, the null hypothesis cannot be rejected, suggesting that the two samples may come from the same underlying distribution. The result of the K-S test ($D = 0.11 < D_{\text{critical}} = 0.12$) shows the two samples are not different at a significant level of 0.05. It indicates that the method captures the main characteristics of local rainfall variability. Therefore, the outputs from the proposed JSR-based method are considered suitable for subsequent temporal downscaling and applications.

Table 1. Best-fit distribution and the associated parameter.

Variable	Source	Distribution	Parameter Value
Rainfall intensity I	Observation	Pearson 3	0.60, 8.20, 5.08, 2.58
	Downscaled results	Pearson 3	0.57, 4.64, 5.06, 2.65
Rainfall duration D	Observation	Pearson 3	0.54, 7.35, 0.74, 2.71
	Downscaled results	Pearson 3	0.44, 5.87, 0.88, 3.01
Annual number of rainfall events N	Observation	Poisson	$\lambda = 20.6$
	Downscaled results	Poisson	$\lambda = 21.8$
Correlation between I and D	Observation	Gaussian	−0.11
	Downscaled results	Gaussian	−0.16

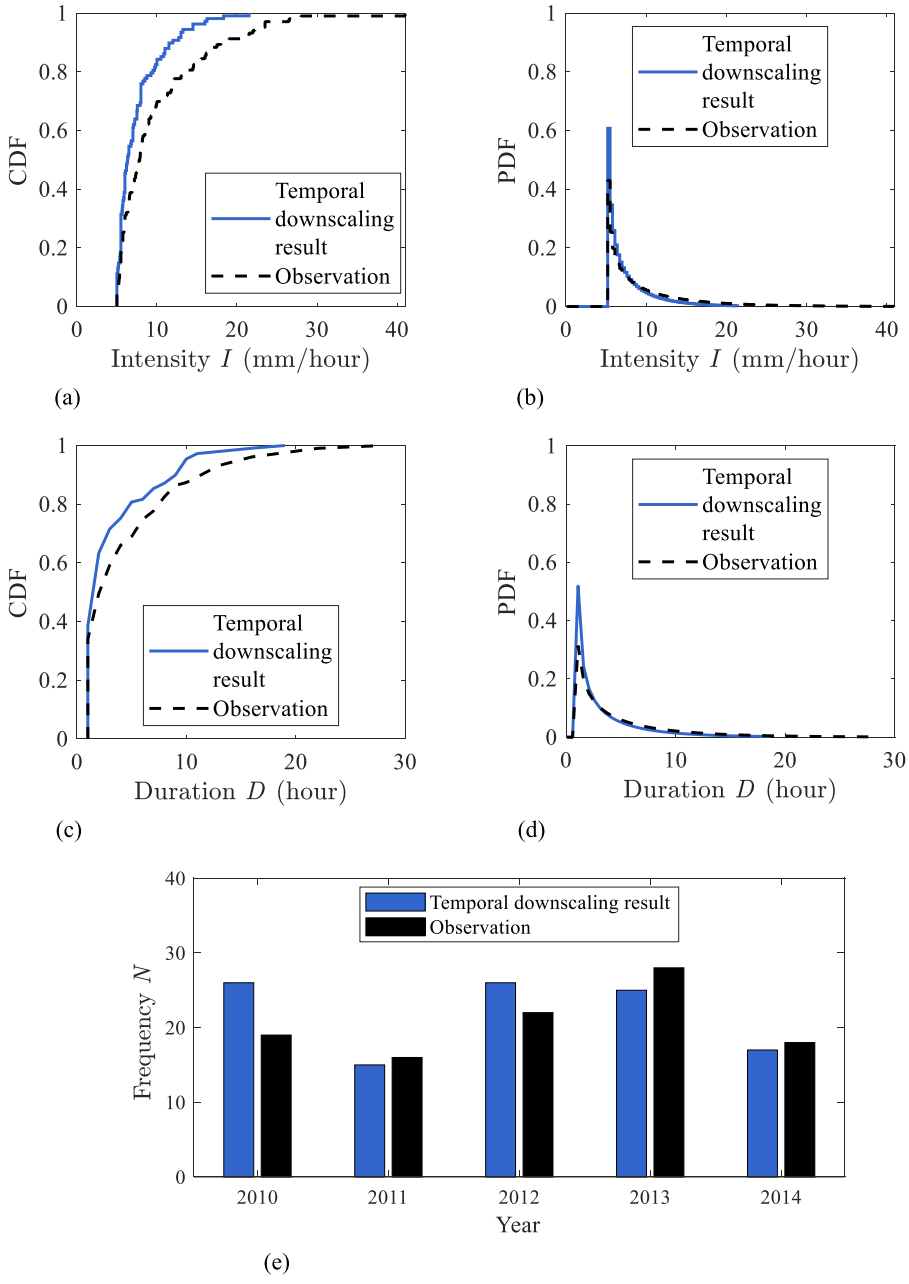

Figure 16. Comparison of characteristics of temporally downscaled rainfall events with observation (January 2010–December 2014) (a) Comparison of intensity CDF (b) Comparison of fitted intensity PDF (c) Comparison of duration CDF (d) Comparison of fitted duration PDF (e) Histogram of rainfall event number frequency.

6.3. Temporal downscaling results and validation (Case 1)

6.3.1. Stochastic storm selection results

In this section, the mean projection of the spatially downscaled results during 2010–2014 is temporally downscaled into hourly rainfall events, which are often needed for evaluating the effect of rainfall on slope stability. Rainfall events with an average intensity ≥ 5 mm/h are considered, as these events might trigger slope instability (Joo et al. 2014; Jun et al. 2017). The characteristics of these events, including intensity (I), duration (D) and annual frequency (N) are fitted individually and a joint distribution of I and D is constructed accordingly (e.g. Liu and Wang 2023). The similarity between the observed and projected distributions of I and D is evaluated using the K–S test and the overall difference between their joint distributions is quantified using the Kullback–Leibler (KL) divergence (Kullback

and Leibler 1951), which is expressed as follows:

$$D_{KL}(P \parallel Q) = \sum_i P(i)\log\left(\frac{P(i)}{Q(i)}\right) \tag{19}$$

where $P(i)$ and $Q(i)$ are the probabilities of event i in the projected and observed joint distributions, respectively.

6.3.2. Validation of temporal downscaling results

Table 1 summarises the best-fitted distribution types and the associated parameters. Figure 16 presents the CDFs of I and D, along with their fitted marginal probability density functions (PDFs). The K – S test results indicate no statistically significant difference between the observed and projected distributions of I and D, indicating that the proposed method captures the statistical characteristics of individual rainfall event properties. Moreover, the joint PDF of I and D is constructed using a copula-based approach to model their dependence structure and the resulting KL divergence is 0.21, indicating a reasonable agreement between the observed and downscaled joint distributions (e.g. Sharma et al. 2024; Zhang et al. 2025). Figure 16 also shows the annual frequency of intense rainfall events over several years. Although the number of events varies from year to year, the estimated Poisson parameter λ, representing the average annual event count, remains comparable between observation and projection (see Table 1). This consistency demonstrates a reasonable performance of the proposed method. At the same time, it should be noted that the tails of the observed rainfall event distributions are constrained by the limited number of rainfall events recorded during 2010–2014 (103 events with intensity ≥ 5 mm/h), corresponding to a minimum probability interval of about 1/103 (≈0.97%). Evaluating goodness-of-fit at smaller probability tails would require longer-term rainfall records, which will be addressed in future studies.

6.4. Future rainfall data time series at N05 (Case 2)

In this section, multiple hourly rainfall projection samples at N05 are generated for a future period of 50 years (2015–2064) under the low-emission scenario SSP1-2.6. Figure 17 presents the hourly rainfall time series of four samples during 2015–2064. It demonstrates that the proposed method can generate

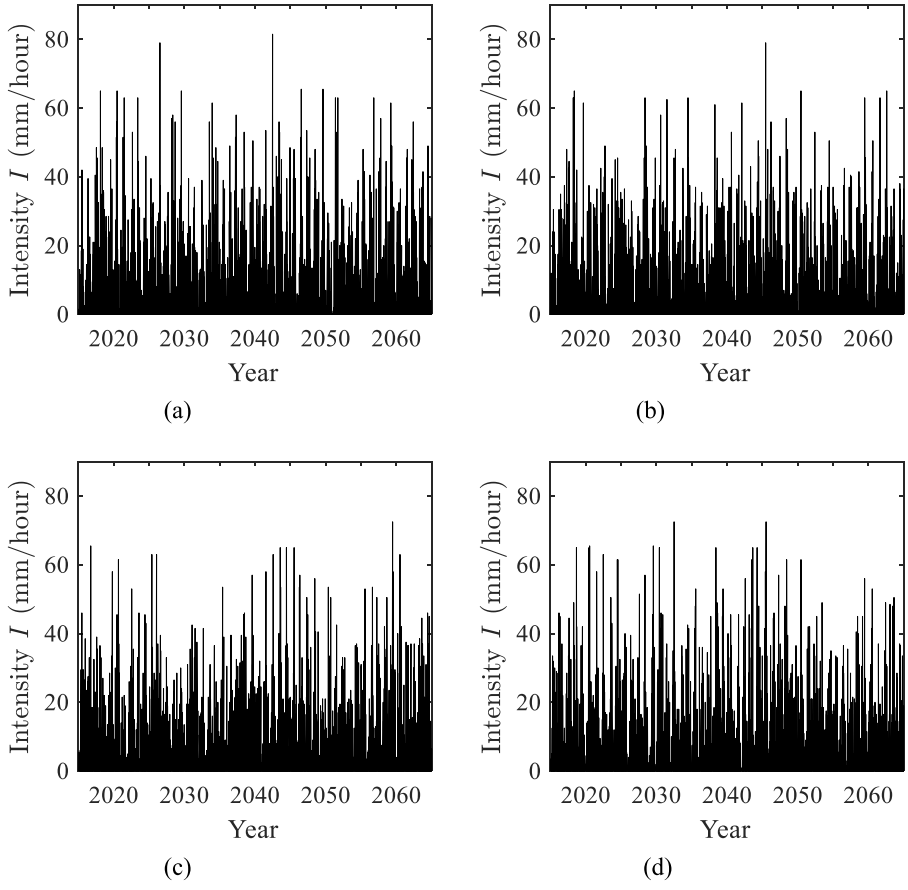

Figure 17. Hourly rainfall data time series of four samples generated by the proposed method at N05 rain gauge (January 2015–December 2064) (a) Sample 1, (b) Sample 2, (c) Sample 3, (d) Sample 4.

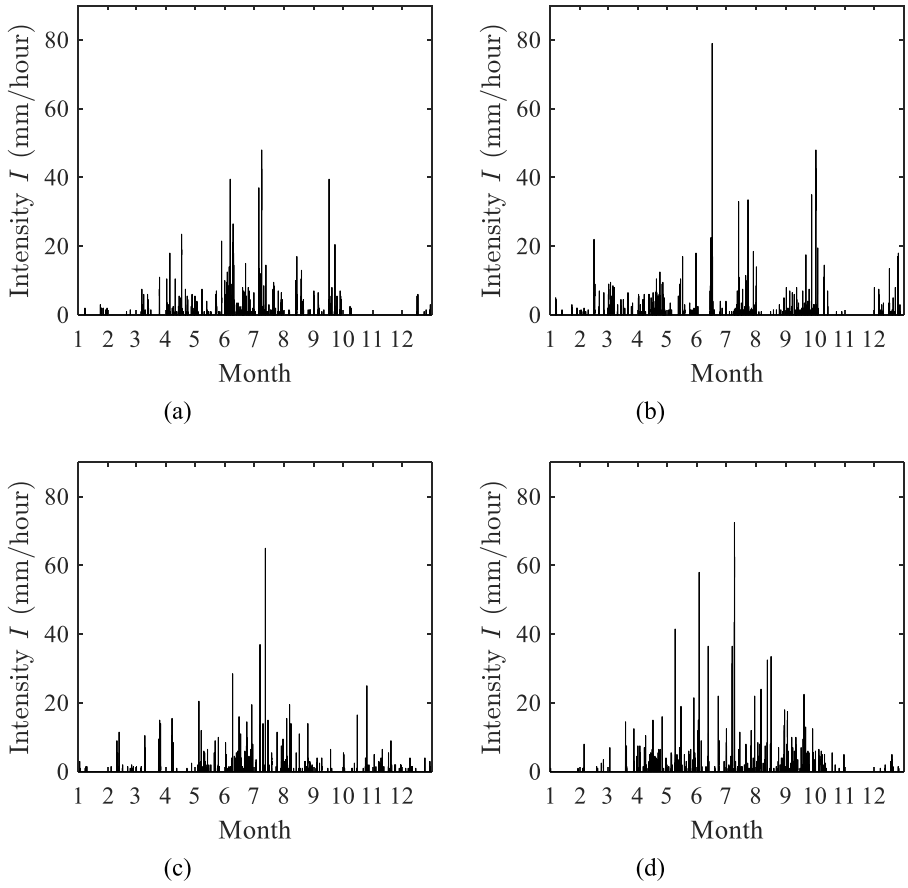

Figure 18. Hourly rainfall data time series of four samples generated by the proposed method at N05 rain gauge for the year 2045 (a) Sample 1, (b) Sample 2, (c) Sample 3, (d) Sample 4.

continuous, long-term, high temporal resolution rainfall series at a specific site, capturing seasonal cycles, inter-annual variability and the occurrence of extreme events. Although the overall seasonal pattern and inter-annual variability are broadly consistent across the samples, differences among the samples in the timing and magnitude of individual events still exist. Since uncertainty in future rainfall cannot be eliminated, the method explicitly represents it by producing multiple plausible realisations of future rainfall, which can be used as input into probabilistic analyses under a Monte Carlo simulation framework. To provide more detailed seasonal rainfall characteristics, Figure 18 shows a zoom-in view for the year 2045 from the same four samples shown in Figure 17. Rainfall is predominantly concentrated between May and October, characterised by frequent intense rainfall events, which can sometimes start in late spring and extend into early autumn. In contrast, the winter months are marked by prolonged dry periods, during which rainfall events are infrequent and generally of low intensity. Notably, despite differences in the timing and magnitude of events among the four samples, all of them consistently exhibit intense rainfall events during the summer, with peak hourly intensities reaching 48, 78, 65 and 72.5 mm/h for Samples 1–4, respectively. Such events are critical for assessing potential hazards, as they can trigger geohazards such as landslides and debris flows. The generated hourly rainfall data time series can be directly employed in engineering analyses, for instance, to define intense rainfall events using inter-event time definition and intensity thresholds, or to construct IDF

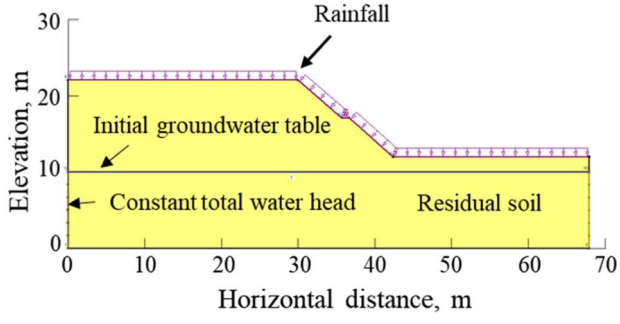

Figure 19. Slope seepage model (after Liu and Wang 2023; Oh and Lu 2015).

Table 2. Slope mechanical and hydraulic parameters (after Liu and Wang 2023).

Parameter	Unit	Residual soil	Shotcrete
Effective cohesion c'	kPa	0	100
Effective friction angle φ'	°	31.6	39
Unit weight	kN/m^3	18.03	22
Residual volumetric water content θ_r	–	0.12	–
Saturated volumetric water content θ_s	–	0.398	–
SWCC model	–	van Genuchten	–
HCF model	–	Modified Mualem	–
SWCC parameter α	kPa^{-1}	0.036	–
SWCC parameter n	–	1.10	–
Saturated hydraulic conductivity K_s	m/s	3.46×10^{-6}	1×10^{-12}

curves to support evaluation of future infrastructure performance under climate change. The proposed method bridges the gap between GCM projections with low spatial and temporal resolutions and site-specific engineering applications.

7. Illustrative slope stability analysis under downscaled projection of future rainfall

To further demonstrate the relevance of the proposed high-resolution rainfall projections for geotechnical applications, a slope stability analysis under future rainfall projections is conducted. A residual soil slope in Pohang, South Korea, previously reported by Oh and Lu (2015) and Liu and Wang (2023), as shown in Figure 19, is adopted as an illustrative example. The slope's seepage model was built in GeoStudio (Krahn 2012) and the corresponding soil parameters are summarised in Table 2.

The future hourly rainfall time series shown in 20(a) generated by the proposed downscaling method is adopted and a rainfall event occurring between 17:00 on 9 June 2045 and 04:00 on 10 June 2045 (see the red line in Figure 20(a)) is imposed on the slope as the infiltration boundary condition. The slope's Factor of Safety (*FS*) is evaluated continuously over the rainfall period as shown in Figure 20(b). The *FS* initially decreases after the onset of rainfall due to infiltration, then shows a slight recovery as rainfall pauses, followed by a further decline with subsequent rainfall. The minimum *FS* of 1.018 is reached at 04:00 on 10 June 2045, indicating that the slope approaches a critical failure condition during this projection. *FS* reduction is highly consistent with variations in rainfall intensity, highlighting the sensitivity of slope stability to the temporal structure of rainfall. Even though the selected event is just one of many possible future realisations, the results illustrate how high-resolution rainfall projections enable explicit examination of rainfall-induced geotechnical responses under climate change. This includes progressive deterioration of slope stability, potentially critical conditions and the timing of critical conditions. High temporal and spatial resolution rainfall projections are therefore essential for quantifying future slope failure risks, supporting early warning systems and informing design and mitigation strategies under climate change scenarios.

8. Summary and conclusions

This study proposes a JSR-based method combined with a stochastic storm selection approach for projecting future hourly rainfall patterns at a specific site. By leveraging both the sparsity and cross – correlation between site-specific rainfall time series and regional GCM projections with a low spatial resolution, the proposed JSR-based method produces reliable site – specific rainfall projections under changing climate conditions. By further integrating a stochastic storm selection method for temporal downscaling, the

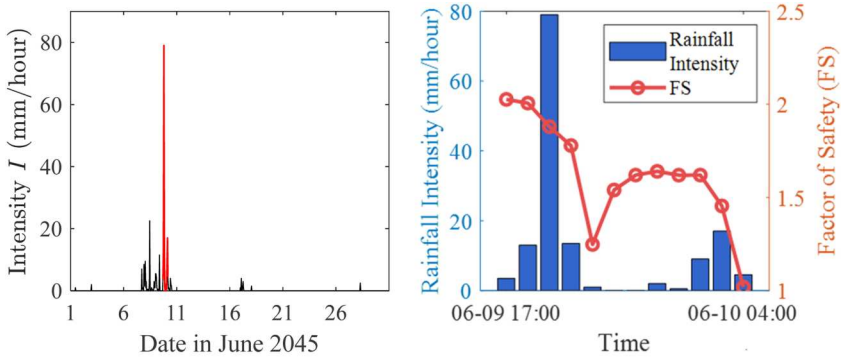

(a) Projected future rainfall time series (b) Factor of Safety (FS) variation during the rainfall event

Figure 20. Rainfall event applied to the slope and the resulting slope stability response (a) Projected future rainfall time series (b) *FS* variation during the rianfall event.

projections are refined into high temporal resolution rainfall events (e.g. hourly) suitable for engineering applications. The whole proposed method was illustrated and validated using N05 rain gauge observations in Hong Kong. Evaluation results show that the method captures key statistical characteristics of rainfall, including seasonality, variability and overall distribution. When projecting future rainfall at N05, the result indicates a possibility of wet conditions under SSP1-2.6, with some projections showing occasional extreme monthly intensities that warrant attention in engineering design.

The proposed method is computationally efficient and data-driven. It bypasses complex physical modelling while effectively capturing both the large-scale non-stationary climate change trends embedded in GCM projections and the local variability from historical site-specific rainfall data time series. Unlike traditional methods, it does not require an explicit functional relationship between GCMs rainfall and local observations, thereby bypassing the issues associated with the non-stationary and highly variable nature of rainfall patterns. In addition, the temporal downscaling after spatial downscaling enables the generation of high – temporal-resolution rainfall data time series suitable for engineering analyses in practice. This is beneficial for real-world engineering applications, such as assessments of rainfall-induced slope instability under climate change.

Disclosure statement

No potential conflict of interest was reported by the author(s).

Funding

The work described in this paper was supported by funding from the State Key Laboratory of Climate Resilience for Coastal Cities at HKUST (project no: ITC-SKLCRCC26EG01) and a grant from the Research Grant Council of the Hong Kong Special Administrative Region (Project No: C7085-24G). The financial support is gratefully acknowledged.

ORCID

Yu Wang http://orcid.org/0000-0003-4635-7059

References

Acharya, S. C., R. Nathan, Q. J. Wang, and C.-H. Su. 2022. "Temporal Disaggregation of Daily Rainfall Measurements Using Regional Reanalysis for Hydrological Applications." *Journal of Hydrology* 610:127867. https://doi.org/10.1016/j.jhydrol.2022.127867.

Ahmed, N., T. Natarajan, and K. R. Rao. 1974. "Discrete Cosine Transform." *IEEE Transactions on Computers* C-23 (1): 90–93. https://doi.org/10.1109/T-C.1974.223784.

Bader, D. C., C. Covey, W. J. Gutowski, I. M. Held, K. E. Kunkel, R. L. Miller, R. T. Tokmakian, and M. H. Zhang. 2008. *Climate Models: An Assessment of Strengths and Limitations (Synthesis and Assessment Product 3.1)*. Washington, DC: U.S. Climate Change Science Program.

Baron, D., M. B. Wakin, M. F. Duarte, S. Sarvotham, and R. G. Baraniuk. 2006. *Distributed Compressed Sensing (Tech. Rep. TREE0612)*. Houston, TX: Rice University.

Bath, B. M. 2012. *Spectral Analysis in Geophysics*. Amsterdam: Elsevier.

Braga, A., and M. Laurini. 2024. "Spatial Heterogeneity in Climate Change Effects across Brazilian Biomes." *Scientific Reports* 14 (1): 16414. https://doi.org/10.1038/s41598-024-67244-x.

Bürger, G., T. Q. Murdock, A. T. Werner, S. R. Sobie, and A. J. Cannon. 2012. "Downscaling Extremes—An Intercomparison of Multiple Statistical Methods for Present Climate." *Journal of Climate* 25 (12): 4366–4388. https://doi.org/10.1175/JCLI-D-11-00408.1.

Candès, E. J., J. Romberg, and T. Tao. 2006. "Robust Uncertainty Principles: Exact Signal Reconstruction from Highly Incomplete Frequency Information." *IEEE Transactions on Information Theory* 52 (2): 489–509. https://doi.org/10.1109/TIT.2005.862083.

Candès, E. J., and M. B. Wakin. 2008. "An Introduction to Compressive Sampling." *IEEE Signal Processing Magazine* 25 (2): 21–30. https://doi.org/10.1109/MSP.2007.914731.

Casella, G., and E. I. George. 1992. "Explaining the Gibbs Sampler." *The American Statistician* 46 (3): 167–174. https://doi.org/10.2307/2685208.

Collison, A., S. Wade, J. Griffiths, and M. Dehn. 2000. "Modelling the Impact of Predicted Climate Change on Landslide Frequency and Magnitude in SE England." *Engineering Geology* 55 (3): 205–218. https://doi.org/10.1016/S0013-7952(99)00121-0.

Daubechies, I. 1992. *Ten Lectures on Wavelets*. Philadelphia, PA: Society for Industrial and Applied Mathematics (SIAM).

Dehn, M., G. Bürger, J. Buma, and P. Gasparetto. 2000. "Impact of Climate Change on Slope Stability Using Expanded Downscaling." *Engineering Geology* 55 (3): 193–204. https://doi.org/10.1016/S0013-7952(99)00123-4.

Deng, L., M. L. Seltzer, D. Yu, A. Acero, A. Mohamed, and G. Hinton. 2013. "Binary Coding of Speech Spectrograms Using a Deep Autoencoder." In *Interspeech 2013*.

Dhanapala Arachchige, S., F. Huang, A. Barton, and B. J. C. Perera. 2014. "Statistical Downscaling of General Circulation Model Outputs to Precipitation—Part 2: Bias-Correction and Future Projections." *International Journal of Climatology* 34 (7): 2155–2169. https://doi.org/10.1002/joc.3915.

Donoho, D. L. 2006. "Compressed Sensing." *IEEE Transactions on Information Theory* 52 (4): 1289–1306. https://doi.org/10.1109/TIT.2006.871582.

Dore, M. H. 2005. "Climate Change and Changes in Global Precipitation Patterns: What Do We Know?" *Environment International* 31 (8): 1167–1181. https://doi.org/10.1016/j.envint.2005.03.004.

Drainage Services Department. 2018. *Stormwater Drainage Manual: Planning, Design and Management*. 5th ed. Hong Kong SAR: Government of the Hong Kong Special Administrative Region.

Duarte, M. F., M. A. Davenport, D. Takhar, J. N. Laska, T. Sun, K. F. Kelly, and R. G. Baraniuk. 2008. "Single-Pixel Imaging via Compressive Sampling." *IEEE Signal Processing Magazine* 25 (2): 83–91. https://doi.org/10.1109/MSP.2007.914730.

Duarte, M. F., and Y. C. Eldar. 2011. "Structured Compressed Sensing: From Theory to Applications." *IEEE Transactions on Signal Processing* 59 (9): 4053–4085. https://doi.org/10.1109/TSP.2011.2161982.

Durack, P. J., K. E. Taylor, P. J. Gleckler, G. A. Meehl, B. N. Lawrence, C. Covey, Ronald J. Stouffer, et al. 2025. "The Coupled Model Intercomparison Project (CMIP): Reviewing Project History, Evolution, Infrastructure and Implementation." *EGUsphere* 2025:1–74. https://doi.org/10.5194/egusphere-2024-3729.

Edwards, R. E. 1982. *Fourier Series: A Modern Introduction, Volume 2*. Vol. 85. New York, NY: Springer.

Elad, M. 2010. *Sparse and Redundant Representations: From Theory to Applications in Signal and Image Processing*. New York, NY: Springer.

Elad, M., and M. Aharon. 2006. "Image Denoising via Sparse and Redundant Representations over Learned Dictionaries." *IEEE Transactions on Image Processing* 15 (12): 3736–3745. https://doi.org/10.1109/TIP.2006.881969.

Fiener, P., and K. Auerswald. 2009. "Spatial Variability of Rainfall on a Sub-Kilometre Scale." *Earth Surface Processes and Landforms* 34 (6): 848–859. https://doi.org/10.1002/esp.1779.

Fornasier, M., and H. Rauhut. 2015. "Compressive Sensing." In *Handbook of Mathematical Methods in Imaging*, edited by O. Scherzer, 205–256. New York, NY: Springer.

Förster, K., F. Hanzer, B. Winter, T. Marke, and U. Strasser. 2016. "An Open-Source Meteorological Observation Time Series Disaggregation Tool (MELODIST v0.1.1)." *Geoscientific Model Development* 9 (7): 2315–2333. https://doi.org/10.5194/gmd-9-2315-2016.

Gao, L., L. Zhang, Y. Hong, H. X. Chen, and S. J. Feng. 2023. "Flood Hazards in Urban Environment." *Georisk: Assessment and Management of Risk for Engineered Systems and Geohazards* 17 (2): 241–261. https://doi.org/10.1080/17499518.2023.2201266.

Gariano, S. L., M. Melillo, S. Peruccacci, and M. T. Brunetti. 2020. "How Much Does the Rainfall Temporal Resolution Affect Rainfall Thresholds for Landslide Triggering?" *Natural Hazards* 100 (2): 655–670. https://doi.org/10.1007/s11069-019-03830-x.

Gofar, N., and L. Min Lee. 2008. "Extreme Rainfall Characteristics for Surface Slope Stability in the Malaysian Peninsular." *Georisk: Assessment and Management of Risk for Engineered Systems and Geohazards* 2 (2): 65–78. https://doi.org/10.1080/17499510802072991.

Guan, Z., and Y. Wang. 2024. "Fusion of Three-Dimensional Geotechnical and Geophysical Data for Developing Digital Twin of Underground Space." *Soils and Foundations* 64 (6): 101528. https://doi.org/10.1016/j.sandf.2024.101528.

Guan, Z., Y. Wang, and K. K. Phoon. 2024. "Fusion of Sparse Non-co-located Measurements from Multiple Sources for Geotechnical Site Investigation." *Canadian Geotechnical Journal* 61 (8): 1574–1592. https://doi.org/10.1139/cgj-2023-0289.

IPCC. 2023. "Sections." In *Climate Change 2023: Synthesis Report. Contribution of Working Groups I, II and III to the Sixth Assessment Report of the Intergovernmental Panel on Climate Change*, edited by H. Lee and J. Romero, 35–115. Geneva: IPCC. https://doi.org/10.59327/IPCC/AR6-9789291691647.

Jeong, D. I., A. St-Hilaire, T. B. M. J. Ouarda, and P. Gachon. 2012. "Multisite Statistical Downscaling Model for Daily Precipitation Combined by Multivariate Multiple Linear Regression and Stochastic Weather Generator." *Climatic Change* 114:567–591. https://doi.org/10.1007/s10584-011-0416-4.

Ji, S., Y. Xue, and L. Carin. 2008. "Bayesian Compressive Sensing." *IEEE Transactions on Signal Processing* 56 (6): 2346–2356. https://doi.org/10.1109/TSP.2007.914345.

Joo, J., J. Lee, J. Kim, H. Jun, and D. J. Jo. 2014. "Inter-event Time Definition Setting Procedure for Urban Drainage Systems." *Water* 6 (1): 45–58. https://doi.org/10.3390/w6010045.

Jun, C., X. Qin, T. Y. Gan, Y. K. Tung, and C. De Michele. 2017. "Bivariate Frequency Analysis of Rainfall Intensity and Duration for Urban Stormwater Infrastructure Design." *Journal of Hydrology* 553:374–383. https://doi.org/10.1016/j.jhydrol.2017.08.004.

Justel, A., D. Peña, and R. Zamar. 1997. "A Multivariate Kolmogorov–Smirnov Test of Goodness of Fit." *Statistics & Probability Letters* 35 (3): 251–259. https://doi.org/10.1016/S0167-7152(97)00020-5.

Koutsoyiannis, D., C. Onof, and H. S. Wheater. 2003. "Multivariate Rainfall Disaggregation at a Fine Timescale." *Water Resources Research* 39 (7): 1–12. https://doi.org/10.1029/2002WR001600.

Krahn, J. 2012. *Seepage Modeling with SEEP/W: An Engineering Methodology*. Calgary: GEO-SLOPE International Ltd.

Kullback, S., and R. A. Leibler. 1951. "On Information and Sufficiency." *The Annals of Mathematical Statistics* 22 (1): 79–86. https://doi.org/10.1214/aoms/1177729694.

Laguardia, G. 2011. "Representing the Precipitation Regime by Means of Fourier Series." *International Journal of Climatology* 31 (9): 1398–1407. https://doi.org/10.1002/joc.2169.

Leung, H. 2024. "Hong Kong Eyes Reopening of Sai Kung Road by Monday after City Sees First Red Rainstorm of Year." Hong Kong Free Press, May 6, 2024. https://hongkongfp.com/2024/05/06/hong-kong-eyes-reopening-of-sai-kung-road-by-monday-after-city-sees-first-red-rainstorm-of-year/.

Liu, X., and Y. Wang. 2023. "Analytical Solutions for Annual Probability of Slope Failure Induced by Rainfall at a Specific Slope Using Bivariate Distribution of Rainfall Intensity and Duration." *Engineering Geology* 313:106969. https://doi.org/10.1016/j.enggeo.2022.106969.

Liu, X., and Y. Wang. 2024. "Quantifying Impacts of Precipitation Scenarios Projected under Climate Change on Annual Probability of Rainfall-Induced Landslides at a Specific Slope." *Computers and Geotechnics* 167:106063. https://doi.org/10.1016/j.compgeo.2023.106063.

Mallat, S. 1999. *A Wavelet Tour of Signal Processing*. San Diego, CA: Elsevier.

Maraun, D., F. Wetterhall, A. M. Ireson, R. E. Chandler, E. J. Kendon, M. Widmann, S. Brienen, H. W. Rust, T. Sauter, M. Themeßl, et al. 2010. "Precipitation Downscaling under Climate Change: Recent Developments to Bridge the Gap between Dynamical Models and the End User."

Reviews of Geophysics 48 (3): 1–24. https://doi.org/10.1029/2009RG000314.

Martel, J.-L., F. P. Brissette, P. Lucas-Picher, M. Troin, and R. Arsenault. 2021. "Climate Change and Rainfall Intensity–Duration–Frequency Curves: Overview of Science and Guidelines for Adaptation." *Journal of Hydrologic Engineering* 26 (10): 03121001. https://doi.org/10.1061/(ASCE)HE.1943-5584.0002122.

Masson-Delmotte, V., P. Zhai, A. Pirani, S. L. Connors, C. Péan, S. Berger, N. Caud, Y. Chen, L. Goldfarb, M. I. Gomis, et al. 2021. *Climate Change 2021: The Physical Science Basis. Contribution of Working Group I to the Sixth Assessment Report of the Intergovernmental Panel on Climate Change*. Vol. 2 (1): 2391. Cambridge: Cambridge University Press. https://doi.org/10.1017/9781009157896.

Mayer, S., C. Fox Maule, S. Sobolowski, O. Bøssing Christensen, H. J. Danielsen Sørup, M. Antonia Sunyer, K. Arnbjerg-Nielsen, and I. Barstad. 2022. "Identifying Added Value in High-Resolution Climate Simulations over Scandinavia." *Tellus A: Dynamic Meteorology and Oceanography* 67 (1): 24941. https://doi.org/10.3402/tellusa.v67.24941.

Müller, H., and U. Haberlandt. 2018. "Temporal Rainfall Disaggregation Using a Multiplicative Cascade Model for Spatial Application in Urban Hydrology." *Journal of Hydrology* 556:847–864. https://doi.org/10.1016/j.jhydrol.2016.01.031.

Narasimhan, T. N. 1999. "Fourier's Heat Conduction Equation: History, Influence, and Connections." *Reviews of Geophysics* 37 (1): 151–172. https://doi.org/10.1029/1998RG900006.

Nerini, D., N. Besic, I. Sideris, U. Germann, and L. Foresti. 2017. "A Non-stationary Stochastic Ensemble Generator for Radar Rainfall Fields Based on the Short-Space Fourier Transform." *Hydrology and Earth System Sciences* 21 (6): 2777–2797. https://doi.org/10.5194/hess-21-2777-2017.

Nissen, K. M., and U. Ulbrich. 2017. "Increasing Frequencies and Changing Characteristics of Heavy Precipitation Events Threatening Infrastructure in Europe under Climate Change." *Natural Hazards and Earth System Sciences* 17 (7): 1177–1190. https://doi.org/10.5194/nhess-17-1177-2017.

Oguz, E. A., R. E. Benestad, K. M. Parding, I. Depina, and V. Thakur. 2024. "Quantification of Climate Change Impact on Rainfall-Induced Shallow Landslide Susceptibility: A Case Study in Central Norway." *Georisk: Assessment and Management of Risk for Engineered Systems and Geohazards* 18 (2): 467–490. https://doi.org/10.1080/17499518.2023.2283848.

Oh, S., and N. Lu. 2015. "Slope stability analysis under unsaturated conditions: Case studies of rainfall-induced failure of cut slopes." *Engineering Geology* 184:96–103. https://doi.org/10.1016/j.enggeo.2014.11.007.

Ohba, M., and S. Sugimoto. 2019. "Differences in Climate Change Impacts between Weather Patterns: Possible Effects on Spatial Heterogeneous Changes in Future Extreme Rainfall." *Climate Dynamics* 52 (7): 4177–4191. https://doi.org/10.1007/s00382-018-4374-1.

Oppenheim, A. V. 1999. *Discrete-Time Signal Processing*. 2nd ed. Upper Saddle River, NJ: Prentice Hall.

Peleg, T., Y. C. Eldar, and M. Elad. 2012. "Exploiting Statistical Dependencies in Sparse Representations for Signal Recovery." *IEEE Transactions on Signal Processing* 60 (5): 2286–2303. https://doi.org/10.1109/TSP.2011.

Rao, K. R., and P. Yip. 2014. *Discrete Cosine Transform: Algorithms, Advantages, Applications*. Boston, MA: Academic Press.

Rashid, M. M., S. Beecham, and R. K. Chowdhury. 2015. "Assessment of Trends in Point Rainfall Using Continuous Wavelet Transforms." *Advances in Water Resources* 82:1–15. https://doi.org/10.1016/j.advwatres.2015.04.006.

Robert, C. P. 2014. *Bayesian Data Analysis*. 3rd ed. Boca Raton, FL: CRC Press.

Sandryhaila, A., and J. M. Moura. 2014. "Big Data Analysis with Signal Processing on Graphs: Representation and Processing of Massive Data Sets with Irregular Structure." *IEEE Signal Processing Magazine* 31 (5): 80–90. https://doi.org/10.1109/MSP.2014.2329213.

Segond, M. L., N. Neokleous, C. Makropoulos, C. Onof, and C. Maksimovic. 2007. "Simulation and Spatio-Temporal Disaggregation of Multi-site Rainfall Data for Urban Drainage Applications." *Hydrological Sciences Journal* 52 (5): 917–935. https://doi.org/10.1623/hysj.52.5.917.

Sharma, A., H. Wang, J. Zhang, M. Lu, and C. Wu. 2024. "Constructing Multivariate Distribution of Rainfall Characteristics: A Bayesian Vine Algorithm." *Journal of Hydrology* 637:131392. https://doi.org/10.1016/j.jhydrol.2024.131392.

Socolofsky, S., E. E. Adams, and D. Entekhabi. 2001. "Disaggregation of Daily Rainfall for Continuous Watershed Modeling." *Journal of Hydrologic Engineering* 6:300–309. https://doi.org/10.1061/(ASCE)1084-0699(2001)6:4(300).

Stankovic, L., E. Sejdic, S. Stankovic, M. Dakovic, and I. Orovic. 2019. "A Tutorial on Sparse Signal Reconstruction and Its Applications in Signal Processing." *Circuits, Systems, and Signal Processing* 38:1206–1263. https://doi.org/10.1007/s00034-018-0909-2.

Stein, E. M., and R. Shakarchi. 2003. *Fourier Analysis: An Introduction*. Princeton, NJ: Princeton University Press.

Strang, G. 1999. "The Discrete Cosine Transform." *SIAM Review* 41 (1): 135–147. https://doi.org/10.1137/S0036144598347302.

Takhellambam, B. S., P. Srivastava, J. Lamba, R. P. McGehee, H. Kumar, and D. Tian. 2022. "Temporal Disaggregation of Hourly Precipitation under Changing Climate over the Southeast United States." *Scientific Data* 9 (1): 211. https://doi.org/10.1038/s41597-022-01304-7.

Tipping, M. E. 2001. "Sparse Bayesian Learning and the Relevance Vector Machine." *Journal of Machine Learning Research* 1:211–244. https://doi.org/10.1162/15324430152748236.

van den Enden, A. W. M., and N. A. M. Verhoeckx. 1989. *Discrete-Time Signal Processing*. Boston, MA: Prentice Hall.

Wallace, J. M., and R. E. Dickinson. 1972. "Empirical Orthogonal Representation of Time Series in the Frequency Domain. Part I: Theoretical Considerations." *Journal of Applied Meteorology* 11 (6): 887–892. https://doi.org/10.1175/1520-0450(1972)011<0887:EOROTS>2.0.CO;2.

Wang, Y., Y. Hu, and K. K. Phoon. 2022. "Non-parametric Modelling and Simulation of Spatiotemporally Varying Geo-Data." *Georisk: Assessment and Management of Risk for Engineered Systems and Geohazards* 16 (1): 77–97. https://doi.org/10.1080/17499518.2021.1971258.

Westra, S., R. Mehrotra, A. Sharma, and R. Srikanthan. 2012. "Continuous Rainfall Simulation: 1. A Regionalized Subdaily Disaggregation Approach." *Water Resources Research* 48 (1): W01535-1–W01535-16. https://doi.org/10.1029/2011WR010489.

Wilby, R. L., S. P. Charles, E. Zorita, B. Timbal, P. H. Whetton, and L. Mearns. 2004. *Guidelines for Use of Climate Scenarios Developed from Statistical Downscaling Methods*. Supporting material of the Intergovernmental Panel on Climate Change. https://api.semanticscholar.org/CorpusID:17449064.

Wilby, R. L., and T. M. L. Wigley. 1997. "Downscaling General Circulation Model Output: A Review of Methods and Limitations." *Progress in Physical Geography: Earth and Environment* 21 (4): 530–548. https://doi.org/10.1177/030913339702100403.

Wong, G., D. Maraun, M. Vrac, M. Widmann, J. M. Eden, and T. Kent. 2014. "Stochastic Model Output Statistics for Bias Correcting and Downscaling Precipitation including Extremes." *Journal of Climate* 27:6940–6959. https://doi.org/10.1175/JCLI-D-13-00604.1.

Wong, K.-h., M.-h. Fan, and H.-y. Yeung. 2024. *Extreme Rainfall Events in Hong Kong*. Hong Kong SAR: Hong Kong Observatory.

Wright, J., Y. Ma, J. Mairal, G. Sapiro, T. S. Huang, and S. Yan. 2010. "Sparse Representation for Computer Vision and Pattern Recognition." *Proceedings of the IEEE* 98 (6): 1031–1044. https://doi.org/10.1109/JPROC.2010.2044470.

Xavier, D. R., C. Barcellos, and C. M. de Freitas. 2014. "Extreme Weather Events and Their Consequences on Health: The 2008 Disaster in Santa Catarina Taking into Account Different Information Sources." *Ambiente & Sociedade* 17:273–294. https://doi.org/10.1590/1809-4422ASOC1119V1742014.

Yiou, P., E. Baert, and M. F. Loutre. 1996. "Spectral Analysis of Climate Data." *Surveys in Geophysics* 17:619–663. https://doi.org/10.1007/BF01931784.

Zhang, J., B. Yang, M. Lu, and A. Sharma. 2025. "Assessing Annual Failure Probability of Soil Slopes under Rainfall and Evaporation." *Computers and Geotechnics* 187:107517. https://doi.org/10.1016/j.compgeo.2025.107517.

Zhang, Z., Y. Xu, J. Yang, X. Li, and D. Zhang. 2015. "A Survey of Sparse Representation: Algorithms and Applications." *IEEE Access* 3:490–530. https://doi.org/10.1109/ACCESS.2015.2430359.

Zhao, T., and Y. Wang. 2020. "Non-parametric Simulation of Non-stationary Non-Gaussian 3D Random Field Samples Directly from Sparse Measurements Using Signal Decomposition and Markov Chain Monte Carlo (MCMC) Simulation." *Reliability Engineering & System Safety* 203:107087. https://doi.org/10.1016/j.ress.2020.107087.